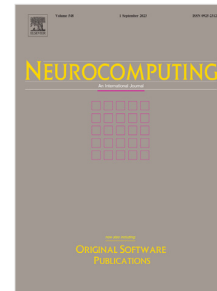


Journal Pre-proof

A unified formulation of geometry-aware discrete dynamic movement primitives

Fares J. Abu-Dakka, Matteo Saveriano, Ville Kyrki



PII: S0925-2312(24)00827-0
DOI: <https://doi.org/10.1016/j.neucom.2024.128056>
Reference: NEUCOM 128056

To appear in: *Neurocomputing*

Received date: 7 August 2023
Revised date: 6 June 2024
Accepted date: 10 June 2024

Please cite this article as: F.J. Abu-Dakka, M. Saveriano and V. Kyrki, A unified formulation of geometry-aware discrete dynamic movement primitives, *Neurocomputing* (2024), doi: <https://doi.org/10.1016/j.neucom.2024.128056>.

This is a PDF file of an article that has undergone enhancements after acceptance, such as the addition of a cover page and metadata, and formatting for readability, but it is not yet the definitive version of record. This version will undergo additional copyediting, typesetting and review before it is published in its final form, but we are providing this version to give early visibility of the article. Please note that, during the production process, errors may be discovered which could affect the content, and all legal disclaimers that apply to the journal pertain.

© 2024 The Author(s). Published by Elsevier B.V. This is an open access article under the CC BY-NC-ND license (<http://creativecommons.org/licenses/by-nc-nd/4.0/>).

A Unified Formulation of Geometry-aware Discrete Dynamic Movement Primitives

Fares J. Abu-Dakka^{a,*}, Matteo Saveriano^b, Ville Kyrki^c

^a*Electronic and Computer Science Department, Faculty of Engineering, Mondragon Unibertsitatea, 20500 Arrasate, Spain*

^b*Automatic Control Lab, Department of Industrial Engineering, University of Trento, Trento, Italy.*

^c*Intelligent Robotics Group, Department of Electrical Engineering and Automation at Aalto University, Aalto, Finland.*

Abstract

Learning from demonstration (LfD) is considered as an efficient way to transfer skills from humans to robots. Traditionally, LfD has been used to transfer Cartesian and joint positions and forces from human demonstrations. The traditional approach works well for some robotic tasks, but for many tasks of interest, it is necessary to learn skills such as orientation, impedance, and/or manipulability that have specific geometric characteristics. An effective encoding of such skills can be only achieved if the underlying geometric structure of the skill manifold is considered and the constraints arising from this structure are fulfilled during both learning and execution. However, typical learned skill models such as dynamic movement primitives (DMPs) are limited to Euclidean data and fail in correctly embedding quantities with geometric constraints. In this paper, we propose a novel and mathematically principled framework that uses concepts from Riemannian geometry to allow DMPs to properly embed geometric constraints. The resulting DMP formulation can deal with data sampled from any Riemannian manifold including, but not limited to, unit quaternions and symmetric and positive definite matrices. The proposed approach has been extensively evaluated both on simulated data and real robot experiments. The performed evaluation demonstrates that beneficial properties of DMPs, such as convergence to a given goal and the possibility to change the goal during operation, apply also to the proposed formulation.

Keywords: Motor control of artificial systems, Movement primitives theory, Dynamic movement primitives, Learning from demonstration, Riemannian manifolds

1. Introduction

Reliable execution of robotic tasks in highly unstructured and dynamic scenarios is fundamental to bringing robots into human-inhabited environments. In such environments, robots need to accurately control their motion in free space as well as during physical interactions, which requires the capability to generate and adapt online reference behaviors in the form of motion, impedance, and/or force trajectories. Therefore, an effective encoding of diverse trajectory data is the key to spreading robotic solutions in everyday environments.

The Learning from Demonstration (LfD) paradigm [1] aims to develop learning solutions that allow the

robot to enrich its skills via human guidance. Among the existing approaches [2, 3], the idea of encoding robotic skills into stable dynamical systems has gained interest in the LfD community [4, 5, 6]. Dynamic Movement Primitives (DMPs) [7] are one of the first and most popular dynamical system-based approaches for LfD. DMPs are capable of encoding both discrete and periodic robotic skills into time-dependent systems. Discrete skills, also referred to as point-to-point motions, consist of motion trajectories with a fixed start and end point (goal) and are well-suited to represent many human daily tasks such as picking and placing objects.

The original DMP formulation considers one Degree of Freedom (DoF) trajectories. Multi-DoF trajectories are learned separately for each DoF and synchronized by a common phase variable. This strategy is effective for encoding independent skills like joint or Cartesian position trajectories, but it fails if the different DoFs are mutually dependent. This situation is common in

*Corresponding author

Email addresses: fabudakka@mondragon.edu

(Fares J. Abu-Dakka), matteo.saveriano@unitn.it

(Matteo Saveriano), ville.kyrki@aalto.fi (Ville Kyrki)

robotics, where variables of interest may be interrelated by geometric constraints. Examples of such variables include: (i) orientation representations, like rotation matrices [8] or unit quaternions [8, 9, 10], and (ii) inertia [11], manipulability [12, 13, 14], stiffness, and damping [15, 16] that are encapsulated in Symmetric Positive Definite (SPD) matrices. For variables interrelated by geometric constraints, the embedding strategy has to be modified to fulfill the constraints during both training and execution.

Several robotic skills consist of a combination of variables belonging to different manifolds. A simple example is a pose trajectory where the position lies in Cartesian space and the orientation is represented *e.g.*, as unit quaternions. To avoid accuracy loss, Riemannian metrics should be embedded in the DMP formulation, allowing the consideration of all the constraints arising from various geometric structures in a unified and consistent manner. This is not possible with existing DMP formulations [4, 8, 9, 17, 18], which are space-dependent.

In this paper, we propose Geometry-aware DMP (\mathcal{G} -DMP), a new formulation that uses differential geometry to extend classical DMP for Euclidean data to other Riemannian manifolds. This extension allows discrete DMPs to effectively represent data evolving on different Riemannian manifolds, which subsequently allows the generation of smooth trajectories for data that do not belong to the Euclidean space. The formulation allows to encode various forms of point-to-point manipulation skills with specific geometric constraints in a unified and manifold independent manner. The general formulation provided in this paper can be applied to any trajectory of data by considering the corresponding Riemannian manifold. The effectiveness of the proposed approach is demonstrated both on synthetic data and physical experimental setups.

Preliminary results of this work have been published in [18], where we formulated DMP equations to learn SPD data profiles. This paper adds several significant novel contributions with respect to our published work:

1. A unified and mathematically principled framework, \mathcal{G} -DMP, that uses differential geometry to extend classical DMPs to any Riemannian manifold.
2. Exploitation of manifold composites to encode and learn composite manifolds in one single DMP formulation.
3. Proof of the stability of the proposed \mathcal{G} -DMP.
4. Formulation of \mathcal{G} -DMP goal switching without the need to use parallel transport.
5. An extensive evaluation and comparison with existing approaches.
6. Instructive and unified source codes accompany the paper with all necessary datasets at <https://gitlab.com/geometry-aware/ga-dmp>.

This paper is organized as follows: Next section presents the state-of-the-art. A background about standard DMPs and Riemannian geometry are given in Sec. 3. Afterwards, we provide the theoretical foundation of \mathcal{G} -DMPs in Sec. 4. Subsequently, we evaluate our approach in several experiments (Sec. 5). The work is concluded in Sec. 6.

2. Related Works

LfD is a valuable framework to teach the robot new skills without explicitly coding them. LfD framework is effective in extracting relevant patterns from a few task demonstrations and in generalizing these patterns to different scenarios. LfD has been deeply investigated and several approaches have been developed in the literature. These include, among others, DMP [4, 20], Probabilistic Movement Primitives (ProMP) [21], Gaussian Mixture Models (GMMs) [22], and Kernelized Movement Primitives (KMP) [10, 23].

In many previous works, training data are simply treated as time series of Euclidean vectors. Other approaches, like [24] and [25], learn and adapt quaternion trajectories without enforcing the unit norm constraint, which leads to non-unit quaternions and hence requires an additional re-normalization step. Nevertheless, several works in the literature have investigated, to some extent, the problem of learning manipulation skills with specific geometric constraints. Examples of such skills include orientations, impedance, and manipulability matrices that are encapsulated in SPD matrices. The following paragraphs examine the state-of-the-art approaches.

DMP-based approaches: For instance, Abudakka *et al.* extended the classical DMPs to encode discrete [17] and periodic [26] unit quaternion trajectories, while the work in [8] also considers different formulation to cope with rotation matrices. The quaternion-based DMPs were also extended to include the real-time goal switching mechanism [8]. The stability of the orientation DMPs is shown in [19]. In [9], authors proposed a modified formulation of unit quaternion DMPs to prevent oscillations that may arise in some cases.

Table 1: Comparison among the state-of-the-art of DMP-based approaches and our \mathcal{G} -DMP across different Riemannian manifolds: Euclidean space of dimension m \mathcal{R}^m , unit quaternion space \mathcal{S}^3 , m -unit sphere manifold \mathcal{S}^m , 3D-rotation matrices space $SO(3)$, special orthogonal group in m dimensions $SO(m)$, and the space of $m \times m$ SPD matrices \mathcal{S}_{++}^m .

	\mathcal{R}^m	\mathcal{S}^3	\mathcal{S}^m	$SO(3)$	$SO(m)$	\mathcal{S}_{++}^m	Composite spaces <i>e.g.</i> , $\mathcal{S}^3 \times \mathcal{R}^3$
Ijspeert <i>et al.</i> [4, 7]	✓	-	-	-	-	-	-
Ude <i>et al.</i> [8]	-	✓	-	✓	-	-	-
Koutras <i>et al.</i> [9], Abu-Dakka <i>et al.</i> [17], Saveriano <i>et al.</i> [19]	-	✓	-	-	-	-	-
Abu-Dakka <i>et al.</i> [18]	-	-	-	-	-	✓	-
Our \mathcal{G} -DMP	✓	✓	✓	✓	✓	✓	✓

130 Abu-Dakka and Kyrki [18] reformulated DMPs to generate discrete SPD profiles, which is also able to adapt
131 to a new goal-SPD-point. There is an important conceptual
132 difference, about how we fit a curve to data points
133 of a demonstration on a manifold, between \mathcal{G} -DMP and
134 our previous work [18]. In [18], to fit a curve to data
135 points $\{\mathbf{P}_i\}_{i=0}^T$ on a Riemannian manifold \mathcal{M} , we sought
136 a curve $\gamma : [t_0, t_T] \rightarrow \mathcal{M}$ that passed exactly through
137 each point of the demonstration trajectory. That assumption
138 does not guarantee proximity between each
139 pair of consecutive points, and, as detailed in Sec. 4.1,
140 this led to the need to use parallel transport to accurately
141 compute the *covariance derivative*. However, in
142 this paper, inspired by [27], we look for γ to be sufficiently
143 straight while passing sufficiently close to the
144 data points at the given intervals. This lets us remove
145 the parallel transport operation, i.e., to approximate the
146 covariant derivative with the total derivative, resulting
147 in a more compact formulation and a more efficient
148 implementation of \mathcal{G} -DMP.

149 Finally, unlike our unified formulation, the formulations
150 of all these previously mentioned approaches are space-specific
151 and do not consider the possibility of treating data from
152 different manifolds in a unified and consistent manner.
153 Table 1 compares our proposed \mathcal{G} -DMP and the state-of-the-art
154 of the DMP-based approaches.

155 **Alternative approaches:** Point-to-point motions are
156 of particular interest in robotics as they form the basis
157 of many everyday manipulation tasks. Therefore, researchers
158 have developed approaches alternative to DMPs to represent
159 point-to-point motions. Focusing on variable orientation
160 profiles, [28] extended GMMs to represent the distribution
161 of the quaternion displacements. Starting from this
162 extended GMM, the work in [29] exploits the Riemannian
163 structure of the unit sphere to encode variable orientations
164 into a geometry-aware Task-Parameterized GMM (TP-GMM)
165 [22]. KMP are extended to unit quaternions in [10] by
166 projecting orientation data onto the tangent space of the
167 unit sphere (which is locally Euclidean). Learning is
168 performed in the tangent space and generated data are
169 projected back to the manifold.

170 SPD matrices are used to encapsulate data in many
171 applications, including brain-computer interfaces [30],
172 transfer learning [31], diffusion tensor imaging [32], as
173 well as various robotic skills [33]. Alternative to DMP,
174 the method in [34] used a tensor-based formulation of
175 GMM and Gaussian Mixture Regression (GMR) on the
176 SPD that enabled learning and reproducing skills involving
177 SPD without additional data re-parametrization.
178 Recently, [14] proposed a kernelized treatment to learn
179 and adapt SPD profiles in the tangent space of the SPD
180 manifold.

181 **\mathcal{G} -DMP vs. state-of-the-art:** The aforementioned
182 geometry-aware formulations are space-specific and do
183 not consider the possibility of treating data from different
184 manifolds in a unified and consistent manner. On the
185 contrary, our \mathcal{G} -DMP formulation is general and can
186 be applied to any trajectory of data even when different
187 DoFs belong to different spaces. Moreover, DMPs are
188 one of the most popular LfD approaches and many
189 robotics applications rely on them. In this respect,
190 \mathcal{G} -DMP provides a useful framework to let users already
191 familiar with DMPs to develop new applications.

192 **3. Preliminaries**

193 In this section, we briefly introduce the classical
194 formulation of discrete DMPs (Sec. 3.1) and define
195 fundamental operations on Riemannian manifolds (Sec. 3.2).
196 Table 2 summarizes the key notations used in this paper.

3.1. Dynamic Movement Primitives

197 DMP is composed of a system of nonlinear differential
198 equations capable of encoding movements while

Table 2: Key notations. Indices, super/subscripts, constants, and variables have the same meaning over the entire text.

mathcal symbols e.g., \mathcal{M}	\triangleq denote manifolds.	bold mathcal symbols e.g., \mathcal{P}	\triangleq denote trajectories.
capital letter variables e.g., \mathbf{P}	\triangleq denote points in a manifold.	small letter variables e.g., \mathbf{p}	\triangleq denote points in a tangent space.
$\mathcal{T}_{\mathbf{P}}\mathcal{M}$	\triangleq The tangent space of a manifold \mathcal{M} around a point \mathbf{P}	++	\triangleq ++
\mathcal{R}^m	\triangleq Euclidean space of dimension m .	\mathcal{S}^m	\triangleq Sphere manifold of dimension m .
$\mathcal{SO}(m)$	\triangleq Special orthogonal group of dimension m .	$\mathcal{SE}(m)$	\triangleq Special Euclidean group of dimension m .
\mathcal{S}_{++}^m	\triangleq Space of $m \times m$ SPD.	\mathcal{SYM}^m	\triangleq Space of $m \times m$ symmetric matrices.
N	\triangleq # of nonlinear basis functions	i	\triangleq index : $i = 1, 2, \dots, N$
l	\triangleq index : $l = 1, 2, \dots, T$	T	\triangleq Number of samples
y, \dot{y}	\triangleq trajectory data and its 1st derivative in classical DMP	z, \dot{z}	\triangleq scaled velocity and acceleration in \mathcal{G} -DMP
$\mathcal{Y}, \dot{\mathcal{Y}}$	\triangleq trajectory data and its 1st derivative in \mathcal{G} -DMP	$\mathcal{Z}, \dot{\mathcal{Z}}$	\triangleq scaled velocity and acceleration in \mathcal{G} -DMP
$\alpha_z, \beta_z, \alpha_x, \alpha_g$	\triangleq Positive constant gains.	x	\triangleq DMP phase variable.
$f(x), \mathcal{F}(x)$	\triangleq forcing term for different spaces	w_i	\triangleq adjustable weights
Ψ_i	\triangleq Gaussian basis functions	c_i and h_i	\triangleq centers and widths of Ψ_i
$g \in \mathbb{R}$ and $\mathbf{G} \in \mathcal{M}$	\triangleq attractor point (goal) in different spaces	$\hat{\mathcal{Y}} \in \mathcal{M}$	\triangleq new manifold trajectory generated by \mathcal{G} -DMP

guaranteeing convergence to a designated goal point (attractor) [20]. The foundational work on DMPs for discrete, point-to-point, motions was first introduced by Ijspeert *et al.* [7]. However, in order to generate movements adaptable to new situations without inducing excessive accelerations or amplification, Pastor *et al.* introduced some modifications [24]. In this paper, we adopt the formulation proposed by Pastor *et al.* . For a single DoF trajectory y , the DMP system of equations proposed in [24] is described as follows:

$$\tau \dot{z} = \alpha_z(\beta_z(g - y - (g - y_0)x + f(x)) - z), \quad (1)$$

$$\tau \dot{y} = z, \quad (2)$$

$$\tau \dot{x} = -\alpha_x x, \quad (3)$$

where τ is a positive scalar that represents the temporal scaling factor and determines the overall duration of the movement. \dot{y} represents velocity and z denotes scaled velocity. x is a phase variable, governing the dynamical system's evolution towards the attractor point. It is used to avoid explicit time dependency in the formulation. The canonical system, given by (3), is initialized as $x(0) = 1$ and vanishes exponentially¹ as $t \rightarrow \infty$ if the gain $\alpha_x > 0$. β_z and α_z are positive gains that define the dynamical system's behavior. In order to ensure a critically damped system, we choose $\alpha_z = 4\beta_z$. The attractor (goal) point of the movement is denoted by g . This system of equations prevents high accelerations at the beginning of the motion or when the goal is

¹The minimum phase to execute a motion within T_f seconds can be computed through $x(T_f) = \exp(-\frac{\alpha_x}{\tau} T_f)$.

close to the initial state, allowing for the reproduction of motions with the same initial and target states while preventing over-amplifications and trajectory mirroring effects when changing the goal.

The nonlinear forcing term $f(x)$ is classically parameterized as a linear combination of N nonlinear radial basis functions scaled by the phase variable x . $f(x)$ allows the dynamical system to preserve the shape of any smooth trajectory, and subsequently, generate this trajectory from an initial position y_0 to the attractor g . Thus, $f(x)$ is defined as:

$$f(x) = \frac{\sum_{i=1}^N w_i \Psi_i(x)}{\sum_{i=1}^N \Psi_i(x)} x, \quad (4)$$

$$\Psi_i(x) = \exp(-h_i(x - c_i)^2), \quad (5)$$

where w_i are the weights adjusted based on measured data to achieve the desired behavior. $\Psi_i(x)$ are Gaussian basis functions with centers c_i and widths h_i . For a given number of basis functions N , centers c_i and widths h_i are defined as follows:

$$c_i = \exp(-\alpha_x \frac{i-1}{N-1}), \quad h_i = \frac{1}{(c_{i+1} - c_i)^2}, \quad h_N = h_{N-1}$$

where $i = 1, \dots, N$. For each DoF.

In order to control multiple DoFs systems, such as trajectories of joint angles of D DoF manipulator, we consider a separate transformation system (1)-(2) for each of the D DoFs to control. Additionally, we utilize a single canonical system (3) shared across the D transformation systems, which synchronizes their time evolution.

227 3.2. Riemannian manifolds

An m -dimensional manifold is a topological space where each point locally resembles Euclidean space \mathcal{R}^m . A differentiable manifold extends this notion to ensure that at each point, there exists a tangent space. A Riemannian manifold \mathcal{M} is a smooth and differentiable manifold where each tangent space is equipped with a Riemannian metric tensor. This tensor, denoted as $\langle \cdot, \cdot \rangle_{\mathbf{P}}$, is a positive definite inner product defined on the tangent space $\mathcal{T}_{\mathbf{P}}\mathcal{M}$ for every point $\mathbf{P} \in \mathcal{M}$. The Riemannian metric introduces the concept of length on the manifold. By utilizing this metric, we can generalize the notion of a “straight line” between two points by defining a geodesic as the shortest curve that connects two points on a manifold. This geodesic allows for the transportation of vectors between tangent spaces [35, 36]. A geodesic $\gamma(t)$ is defined as a continuously differentiable curve that connects points \mathbf{A}, \mathbf{B} on the manifold \mathcal{M} . It locally minimizes the distance between these points, and its length is given by the functional:

$$\mathcal{L}_{\mathbf{A}}^{\mathbf{B}}(\gamma) = \int_0^1 \langle \dot{\gamma}(t), \dot{\gamma}(t) \rangle dt. \quad (6)$$

The distance between points \mathbf{A} and \mathbf{B} is then defined by minimizing (6), i.e.,

$$\text{dist}(\mathbf{A}, \mathbf{B}) = \min \mathcal{L}_{\mathbf{A}}^{\mathbf{B}}(\gamma) \quad (7)$$

228 3.2.1. Mapping operators

229 The tangent spaces and their bases provide the ability to perform linear algebra. In order to perform computations on the manifold while preserving distances, a mapping system is needed to switch between the tangent space $\mathcal{T}_{\mathbf{P}}\mathcal{M}$ and the manifold \mathcal{M} , see Fig. 1. These mapping operators are:

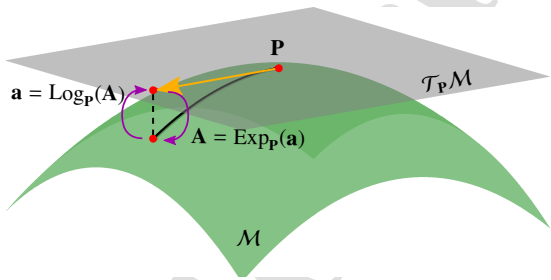


Figure 1: A Riemannian manifold \mathcal{M} and its tangent space $\mathcal{T}_{\mathbf{P}}\mathcal{M}$ defined at point \mathbf{P} .

- **The logarithmic map** ($\text{Log}_{\mathbf{P}}(\cdot)$) is a function that maps a point $\mathbf{A} \in \mathcal{M}$ into a point $\mathbf{a} \in \mathcal{T}_{\mathbf{P}}\mathcal{M}$ (see Fig. 1). It is defined as:

$$\text{Log}_{\mathbf{P}}(\cdot): \mathcal{M} \mapsto \mathcal{T}_{\mathbf{P}}\mathcal{M}, \quad (8)$$

- **The exponential map** ($\text{Exp}_{\mathbf{P}}(\cdot)$) is the inverse of the logarithmic map. It maps a point $\mathbf{a} \in \mathcal{T}_{\mathbf{P}}\mathcal{M}$ in the tangent space of \mathbf{P} to a point $\mathbf{A} \in \mathcal{M}$ such that \mathbf{A} lies on the geodesic starting from \mathbf{P} in the direction of \mathbf{a} with distance of $\|\mathbf{a}\| = \langle \mathbf{a}, \mathbf{a} \rangle_{\mathbf{P}}$ (see Fig. 1). It is defined as:

$$\text{Exp}_{\mathbf{P}}(\cdot): \mathcal{T}_{\mathbf{P}}\mathcal{M} \mapsto \mathcal{M}, \quad (9)$$

235 3.2.2. Cartesian products in Riemannian geometry

236 In Riemannian geometry, the Cartesian product of two Riemannian manifolds \mathcal{M} and \mathcal{N} is also a manifold denoted as $\mathcal{M} \times \mathcal{N}$. This construction allows us to combine the geometric structures of both \mathcal{M} and \mathcal{N} into a single manifold.

237 For any points $\mathbf{P}_1 \in \mathcal{M}$ and $\mathbf{U}_1 \in \mathcal{N}$, and their corresponding tangent vectors $\mathbf{p}_1 \in \mathcal{T}_{\mathbf{P}_1}\mathcal{M}$ and $\mathbf{u}_1 \in \mathcal{T}_{\mathbf{U}_1}\mathcal{N}$, the tangent space of $\mathcal{M} \times \mathcal{N}$ at the point $(\mathbf{P}_1, \mathbf{U}_1)$ is isomorphic to the direct sum of the tangent spaces of \mathcal{M} and \mathcal{N} :

$$\mathcal{T}_{(\mathbf{P}_1, \mathbf{U}_1)}(\mathcal{M} \times \mathcal{N}) \cong \mathcal{T}_{\mathbf{P}_1}\mathcal{M} \oplus \mathcal{T}_{\mathbf{U}_1}\mathcal{N}, \quad (10)$$

242 This means that any tangent vector at $(\mathbf{P}_1, \mathbf{U}_1)$ can be uniquely decomposed into a pair of tangent vectors, one in $\mathcal{T}_{\mathbf{P}_1}\mathcal{M}$ and the other in $\mathcal{T}_{\mathbf{U}_1}\mathcal{N}$.

243 To facilitate computations on the Cartesian product manifold $\mathcal{M} \times \mathcal{N}$, we require to redefine the mapping operators in (8) and (9) as follows:

$$\text{Log}_{(\mathbf{P}_1, \mathbf{U}_1)}(\mathbf{P}_2, \mathbf{U}_2) : \mathcal{M} \times \mathcal{N} \mapsto \mathcal{T}_{(\mathbf{P}_1, \mathbf{U}_1)}(\mathcal{M} \times \mathcal{N}), \quad (11)$$

$$\text{Exp}_{(\mathbf{P}_1, \mathbf{U}_1)}(\mathbf{p}, \mathbf{u}) : \mathcal{T}_{(\mathbf{P}_1, \mathbf{U}_1)}(\mathcal{M} \times \mathcal{N}) \mapsto \mathcal{M} \times \mathcal{N}. \quad (12)$$

244 This leads to

$$\text{Log}_{(\mathbf{P}_1, \mathbf{U}_1)}(\mathbf{P}_2, \mathbf{U}_2) = \text{Log}_{\begin{bmatrix} \mathbf{P}_1 \\ \mathbf{U}_1 \end{bmatrix}} \left(\begin{bmatrix} \mathbf{P}_2 \\ \mathbf{U}_2 \end{bmatrix} \right) = \begin{bmatrix} \text{Log}_{\mathbf{P}_1}(\mathbf{P}_2) \\ \text{Log}_{\mathbf{U}_1}(\mathbf{U}_2) \end{bmatrix},$$

$$\text{Exp}_{(\mathbf{P}_1, \mathbf{U}_1)}(\mathbf{p}, \mathbf{u}) = \text{Exp}_{\begin{bmatrix} \mathbf{P}_1 \\ \mathbf{U}_1 \end{bmatrix}} \left(\begin{bmatrix} \mathbf{p} \\ \mathbf{u} \end{bmatrix} \right) = \begin{bmatrix} \text{Exp}_{\mathbf{P}_1}(\mathbf{p}) \\ \text{Exp}_{\mathbf{U}_1}(\mathbf{u}) \end{bmatrix}.$$

245 where $(\mathbf{p}, \mathbf{u}) \in \mathcal{T}_{(\mathbf{P}_1, \mathbf{U}_1)}(\mathcal{M} \times \mathcal{N})$ and $(\mathbf{P}_2, \mathbf{U}_2) \in \mathcal{M} \times \mathcal{N}$.

250 3.2.3. Computing in Riemannian manifolds

251 Let $\mathbf{P}_1, \mathbf{P}_2 \in \mathcal{M}$ and $\mathbf{p}_1, \mathbf{p}_2 \in \mathcal{R}^m$, then the reinterpretation of basic standard operations (e.g., addition and subtraction) in a Riemannian manifold are summarized in Tab. 3.

Table 3: Re-interpretation of basic standard operations in a Riemannian manifold [37].

	Euclidean space	Riemannian manifold
Subtraction	$\vec{\mathbf{p}}_2 = \mathbf{p}_2 - \mathbf{p}_1$	$\vec{\mathbf{P}}_1 \vec{\mathbf{P}}_2 = \text{Log}_{\mathbf{P}_1}(\mathbf{P}_2)$
Addition	$\mathbf{p}_2 = \mathbf{p}_1 + \vec{\mathbf{p}}_2$	$\mathbf{P}_2 = \text{Exp}_{\mathbf{P}_1}(\vec{\mathbf{P}}_1 \vec{\mathbf{P}}_2)$
Distance	$\text{dist}(\mathbf{p}_1, \mathbf{p}_2) = \ \mathbf{p}_2 - \mathbf{p}_1\ $	$\text{dist}(\mathbf{P}_1, \mathbf{P}_2) = \ \vec{\mathbf{P}}_1 \vec{\mathbf{P}}_2\ _{\mathbf{P}_1}$
Interpolation	$\mathbf{p}(t) = \mathbf{p}_1 + t\vec{\mathbf{p}}_2$	$\mathbf{P}(t) = \text{Exp}_{\mathbf{P}_1}(t\vec{\mathbf{P}}_1 \vec{\mathbf{P}}_2)$

277 goal $\mathbf{G} \in \mathcal{M}$ regardless of the initial starting point \mathbf{Y}_0 .
 278 To achieve this, it is necessary to transform the clas-
 279 sical DMP system described by (1)–(2) into a unified
 280 geometry-aware formulation utilizing principles from
 281 Riemannian geometry. In pursuit of this objective, we
 282 initiate the process by considering the expression of a
 283 general second-order system evolving on a manifold, as
 284 outlined by Fiori *et al.* [39]

3.2.4. Riemannian geometric mean

255 Given a set of points $\{\mathbf{P}_i\}_{i=1}^n \in \mathcal{M}$ and a geodesic
 distance $\text{dist}(\mathbf{P}_j, \mathbf{P}_i)$ between two points in \mathcal{M} , the
 Fréchet mean [38] is estimated by minimizing the sum
 of squared geodesic distances

$$\bar{\mathbf{P}} = \arg \min_{\mathbf{P} \in \mathcal{M}} \sum_{i=1}^N \text{dist}^2(\mathbf{P}, \mathbf{P}_i), \quad (13)$$

256 This estimation can be efficiently computed iteratively
 by following Alg. 1 [38].

Algorithm 1 Intrinsic mean

Initialization: $\bar{\mathbf{P}} = \mathbf{P}_1$

- 1: **while** $\|\mathbf{a}\| < \delta$ **do**
 - 2: $\mathbf{a} = \frac{1}{N} \sum_{i=1}^N \text{Log}_{\bar{\mathbf{P}}}(\mathbf{P}_i)$
 - 3: $\bar{\mathbf{P}} = \text{Exp}_{\bar{\mathbf{P}}}(\epsilon \mathbf{a})$; $\epsilon \leq 1$
 - 4: **end while**
-

257

4. Proposed approach

259 In this section, we provide a generalized and unified
 260 formulation for DMPs based on Riemannian geometry
 261 in order to learn and adapt robot manipulation skills re-
 262 gardless its corresponding space, for example orienta-
 263 tion trajectories ($\mathcal{SO}(3)$ or \mathcal{S}^3), pose data ($\mathcal{SE}(3)$), and
 264 SPD profiles (\mathcal{S}_{++}^n) such as stiffness, manipulability, in-
 265 ertia. We also show that our \mathcal{G} -DMP inherits desirable
 266 properties of the original formulation like convergence
 267 to a target and goal switching.

4.1. Geometry-aware DMPs formulation

269 In this section, we introduce the mathematical founda-
 270 tions of \mathcal{G} -DMP technique. The \mathcal{G} -DMP formula-
 271 tion offers a comprehensive and cohesive approach to
 272 encode and execute a discrete trajectory $\mathcal{Y} = \{t_l, \mathbf{Y}_l\}_{l=0}^T$,
 273 commonly known as a point-to-point trajectory, which
 274 evolves within the confines of a Riemannian manifold
 275 \mathcal{M} , where each $\mathbf{Y}_l \in \mathcal{M}$. Its attractor dynamics on
 276 the manifold guarantee the convergence of \mathcal{Y} toward a

$$\tau \nabla_{\mathcal{Z}} \mathcal{Z} = \mathbf{h}(\mathcal{Z}, \mathcal{Y}, x), \quad (14)$$

$$\tau \dot{\mathcal{Y}} = \mathcal{Z}, \quad (15)$$

where \mathcal{Z} and $\dot{\mathcal{Z}}$ represent the scaled first and second
 derivatives of \mathcal{Y} . The phase variable x is similar to
 the one defined in (1) and (3). The *covariant deriva-*
tive $\nabla_{\mathcal{Z}} \mathcal{Z}$ can be defined from the total derivative $\dot{\mathcal{Z}}$
 using parallel transport [39, 18]. However, computing
 the parallel transport is, in general, time-consuming.
 Assuming that consecutive points on the manifold are
 sufficiently close, and the geodesic between them ap-
 proximates a straight line, the covariant derivative can
 be well approximated by manifold-valued finite differ-
 ences [40, 27]. This approximation significantly sim-
 plifies the computation process while introducing neg-
 ligible errors. Thus, in this work, we consider the ap-
 proximation $\nabla_{\mathcal{Z}} \mathcal{Z} \approx \dot{\mathcal{Z}}$. The function $\mathbf{h}(\cdot)$ may encom-
 pass multiple additive contributions. In this study, we
 assume that

$$\mathbf{h}(\mathcal{Z}, \mathcal{Y}, x) = \alpha_z (\beta_z (\text{Log}_{\mathcal{Y}}(\mathbf{G}) - \text{Log}_{\mathbf{Y}_0}(\mathbf{G})x + \mathcal{F}(x)) - \mathcal{Z}), \quad (16)$$

285 where $\mathbf{G} \in \mathcal{M}$ is the goal point. The function $\text{Log}_{\mathcal{Y}}(\cdot)$
 286 is defined in (8). Additionally, positive gains α_z and β_z
 287 are introduced. The term $-\alpha_z \mathcal{Z}$ represents a *dissipative*
 288 *force* that plays a similar role to damping in a mechan-
 289 ical system. The term $\alpha_z (\beta_z \text{Log}_{\mathcal{Y}}(\mathbf{G}))$ corresponds to
 290 *conservative force* and can be interpreted as the nega-
 291 tive gradient of a potential. This can be demonstrated
 292 by considering that $-\frac{1}{2} \nabla_{\mathcal{Y}} \text{dist}^2(\mathcal{Y}, \mathbf{G}) = \text{Log}_{\mathcal{Y}}(\mathbf{G})$ [39],
 293 where $\text{dist}(\cdot, \cdot)$ denotes the Riemannian distance. Fi-
 294 nally, the term $\mathcal{F}(x)$ represents a phase-dependent forc-
 295 ing term which is learned from the demonstration and
 296 will be further discussed in this section.

Consequently, we can redefine the dynamic system
 presented in (1)–(2) as follows

$$\tau \dot{\mathcal{Z}} = \alpha_z (\beta_z (\text{Log}_{\mathcal{Y}}(\mathbf{G}) - \text{Log}_{\mathbf{Y}_0}(\mathbf{G})x + \mathcal{F}(x)) - \mathcal{Z}). \quad (17)$$

$$\tau \dot{\mathcal{Y}} = \mathcal{Z}, \quad (18)$$

The forcing term $\mathcal{F}(x)$ is defined as follows

$$\mathcal{F}(x) = \frac{\sum_{i=1}^N \mathbf{w}_i \Psi_i(x)}{\sum_{i=1}^N \Psi_i(x)} x, \quad (19)$$

where $\mathbf{w}_i \in \mathcal{R}^{m \times N}$ are the weights (free parameters) that can be estimated by encoding any sampled trajectory (e.g., any robot manipulation skill profile). In order to estimate the parameters of a corresponding \mathcal{G} -DMPs, we need to estimate the 1st and 2nd time derivatives of the demonstrated trajectory. The 1st time derivative is computed as follows

$$\dot{\mathcal{Y}} = \left\{ (\text{Log}_{\mathbf{Y}_{l-1}}(\mathbf{Y}_l)) / \delta t \right\}_{l=1}^T \in \mathcal{T}_{\mathbf{Y}_{l-1}} \mathcal{M}, \quad (20)$$

where $\delta t = t_l - t_{l-1}$. The 2nd-time-derivative $\ddot{\mathcal{Y}}$ can be computed straight forward from $\dot{\mathcal{Y}}$ using standard Euclidean tools, i.e., $\ddot{\mathcal{Y}} = \{t_l, \ddot{\mathbf{y}}_l\}_{l=1}^T$ where $\ddot{\mathbf{y}}_l = (\dot{\mathbf{y}}_l - \dot{\mathbf{y}}_{l-1}) / \delta t$.

Having all necessary data $\{t_l, \mathbf{Y}_l, \dot{\mathbf{y}}_l, \ddot{\mathbf{y}}_l\}$, and by inverting (17), the parameters \mathbf{w}_i and the approximated desired shape of the demonstration are estimated as follows

$$\frac{\sum_{i=1}^N \mathbf{w}_i \Psi_i(x_l)}{\sum_{i=1}^N \Psi_i(x_l)} x_l = \frac{\tau^2 \ddot{\mathbf{y}}_l + \alpha_z \tau \dot{\mathbf{y}}_l}{\alpha_z \beta_z} - \text{Log}_{\mathbf{Y}_l}(\mathbf{G}) + \text{Log}_{\mathbf{Y}_0}(\mathbf{G}) x \quad (21)$$

Using (21), the weights \mathbf{w}_i can be estimated by encoding any sampled robot manipulation skill data.

In the reproduction, equation (18) is integrated using the forward Euler-Riemann stepping method [39] as

$$\hat{\mathcal{Y}}(t + \delta t) = \text{Exp}_{\mathbf{Y}_l} \left(\mathcal{Z}(t) \frac{\delta t}{\tau} \right), \quad (22)$$

where $\hat{\mathcal{Y}} \in \mathcal{M}$ represents the new robot manipulation skills data. Equation (22) is manifold dependent. $\text{Exp}_{\mathbf{Y}_l}(\cdot)$ is defined as in (9), and we refer to the appendix for the expression of $\text{Exp}_{\mathbf{Y}_l}(\cdot)$ for the manifolds used in this work.

In case the manifold is a Lie group, the expression of a general second-order system on a Lie group becomes [39]

$$\tau \dot{\mathcal{Z}} = \mathbf{h}(\mathcal{Z}, \mathcal{Y}, x), \quad (23)$$

$$\tau \dot{\mathcal{Y}} = \mathbf{g}(\mathcal{Z}, \mathcal{Y}), \quad (24)$$

from which is straightforward to derive that

$$\tau \dot{\mathcal{Z}} = \alpha_z \left(\beta_z \left(\text{Log}(\mathbf{Y}_g * \mathcal{Y}^{-1}) - \text{Log}(\mathbf{Y}_g * \mathbf{Y}_0^{-1}) + \mathcal{F}(x) \right) - \mathcal{Z} \right), \quad (25)$$

$$\tau \dot{\mathcal{Y}} = \mathbf{g}(\mathcal{Z}, \mathcal{Y}). \quad (26)$$

Equation (25) is formally the same as (17), provided we use the logarithmic map $\text{Log}_{\mathcal{Y}}(\cdot) = \text{Log}(\mathbf{Y}_g * \mathcal{Y}^{-1})$ defined using Lie group theory. The term $\mathbf{m}(\cdot)$ in (26) is the *inverse left translation*, which maps a tangent vector from the Lie algebra to the tangent space at \mathbf{Y}_l and depends on the specific Lie group. The expressions of $\mathbf{g}(\cdot)$ and $\text{Log}(\cdot)$ for unit quaternions and rotation matrices, two Lie groups commonly used in robotics, are given in Appendix A.3 and Appendix A.5.

As a remark, we used the Riemannian formulation (17)–(18) in the rest of the paper. However, for the sake of completeness, we also have provided a formulation for Lie groups in (25)–(26).

4.2. Goal switching

In many real scenarios, while the robot executes its trajectory, it may encounter situations where it needs to adapt its trajectory to a new goal, e.g., new pick-up point, on the fly. This change of goal, referred to as goal switching, is a common requirement in dynamic environments. In order to achieve smooth transitions between goals and avoid unnecessary jumps, the authors of [4] suggested adding an extra first-order differential equation to gradually transition the current goal g to the new goal g_{new} over time. This differential equation can be written as

$$\tau \dot{g} = \alpha_g (g_{\text{new}} - g), \quad (27)$$

where $\alpha_g > 0$ is a positive constant gain. The gradual transition in (27) ensures that the robot's behavior remains continuous and responsive to changes in its task environment.

Analogously, Riemannian manifold-based \mathcal{G} -DMP can switch the goal using

$$\tau \dot{\mathcal{G}} = \alpha_g \text{Log}_{\mathcal{G}}(\mathbf{G}_{\text{new}}). \quad (28)$$

Equation (28) allows to continuously update \mathbf{G} until it smoothly reaches the new value $\mathbf{G}_{\text{new}} \in \mathcal{M}$.

4.3. Stability analysis

Theorem 1 states the stability conditions of the geometry-aware DMP formulation in Sec. 4.1.

Theorem 1. *Assume that $\mathcal{F}(x) \rightarrow 0$ for $t \rightarrow +\infty$ and that the gains $\alpha_z, \beta_z > 0$. Under these assumptions, the geometry-aware DMP has a globally (in its domain of definition) asymptotically stable equilibrium at $(\mathbf{G}, \mathbf{0})$.*

Proof. Recall that, by assumption, we restrict the domain to the points where the logarithmic map $\text{Log}_{\mathcal{Y}}(\mathbf{G})$ is uniquely defined. Recall also that the forcing term

$\mathcal{F}(x)$ in (17) is a weighted sum of Gaussian basis functions. Therefore, the non-linear terms in (17) and (18) are smooth and uniquely defined functions. Consider also that the time dependency introduced by x vanishes for $t \rightarrow +\infty$. Hence, (17) and (18) are an *asymptotically autonomous differential system* and the stability can be proved by analyzing its asymptotic behavior [41]. This allows us to neglect the terms $\mathcal{F}(x)$ and $\text{Log}_{\mathbf{Y}_0}(\mathbf{G})x$ in the stability analysis and to focus on the asymptotic dynamics

$$\dot{\mathbf{Z}} = \alpha_z \beta_z \text{Log}_{\mathbf{Y}}(\mathbf{G}) - \alpha_z \mathbf{Z}, \quad (29)$$

$$\dot{\mathbf{Y}} = \mathbf{Z}, \quad (30)$$

where we set $\tau = 1$ without loss of generality.

We first show that $(\mathbf{G}, \mathbf{0})$ is an equilibrium point of the system (29) and (30). The right side of (30) vanishes only for $\mathbf{Z} = \mathbf{0}$. With $\mathbf{Z} = \mathbf{0}$, the right side of (29) vanishes only for $\text{Log}_{\mathbf{Y}}(\mathbf{G}) = \mathbf{0} \Leftrightarrow \mathbf{Y} = \mathbf{G}$. This implies that the system (29) and (30) has a unique equilibrium point at $(\mathbf{G}, \mathbf{0})$.

We now show that the equilibrium $(\mathbf{G}, \mathbf{0})$ is a global attractor in the chart where the logarithmic map $\text{Log}_{\mathbf{Y}}(\mathbf{G})$ is uniquely defined. To this end, we define the candidate Lyapunov function

$$V(\mathbf{Y}, \mathbf{Z}) = \text{dist}^2(\mathbf{Y}, \mathbf{G}) + \frac{1}{\alpha_z \beta_z} \langle \mathbf{Z}, \mathbf{Z} \rangle_{\mathbf{Y}}, \quad (31)$$

where $\text{dist}(\cdot, \cdot)$ is the Riemannian distance defined as in (7) and $\langle \cdot, \cdot \rangle_{\mathbf{Y}}$ is the positive definite inner product (see Sec. 3.2). $V(\mathbf{Y}, \mathbf{Z})$ is positive definite everywhere if $\alpha_z \beta_z > 0$ and vanishes only at $\mathbf{Y} = \mathbf{G}$ ($\text{dist}^2(\mathbf{G}, \mathbf{G}) = 0$) and $\mathbf{Z} = \mathbf{0}$ ($\langle \mathbf{0}, \mathbf{0} \rangle_{\mathbf{Y}} = 0$). To show that $V(\mathbf{Y}, \mathbf{Z})$ is a valid Lyapunov function we need to show that its time derivative is negative definite and vanishes at $(\mathbf{G}, \mathbf{0})$. The time derivative of $V(\mathbf{Y}, \mathbf{Z})$ can be written as

$$\begin{aligned} \dot{V}(\mathbf{Y}, \mathbf{Z}) &= \frac{d}{dt} \text{dist}^2(\mathbf{Y}, \mathbf{G}) + \frac{1}{\alpha_z \beta_z} \frac{d}{dt} \langle \mathbf{Z}, \mathbf{Z} \rangle_{\mathbf{Y}} \\ &= -2 \langle \text{Log}_{\mathbf{Y}}(\mathbf{G}), \dot{\mathbf{Y}} \rangle_{\mathbf{Y}} + \frac{2}{\alpha_z \beta_z} \langle \dot{\mathbf{Z}}, \mathbf{Z} \rangle_{\mathbf{Y}} \end{aligned} \quad (32)$$

where we used the expression $\frac{d}{dt} \text{dist}^2(\mathbf{Y}, \mathbf{G}) = -2 \langle \text{Log}_{\mathbf{Y}}(\mathbf{G}), \dot{\mathbf{Y}} \rangle_{\mathbf{Y}}$ from [42] and the bi-linearity and the symmetry of the interior product to write $\frac{d}{dt} \langle \mathbf{Z}, \mathbf{Z} \rangle_{\mathbf{Y}} = 2 \langle \dot{\mathbf{Z}}, \mathbf{Z} \rangle_{\mathbf{Y}}$. By replacing $\dot{\mathbf{Z}}$ from (29) and $\dot{\mathbf{Y}}$ from (30) into (32), we obtain

$$\begin{aligned} \dot{V}(\mathbf{Y}, \mathbf{Z}) &= -2 \langle \text{Log}_{\mathbf{Y}}(\mathbf{G}), \mathbf{Z} \rangle_{\mathbf{Y}} + 2 \langle \text{Log}_{\mathbf{Y}}(\mathbf{G}), \mathbf{Z} \rangle_{\mathbf{Y}} \\ &\quad - \frac{2}{\beta_z} \langle \mathbf{Z}, \mathbf{Z} \rangle_{\mathbf{Y}} = -\frac{2}{\beta_z} \langle \mathbf{Z}, \mathbf{Z} \rangle_{\mathbf{Y}} \leq 0, \end{aligned}$$

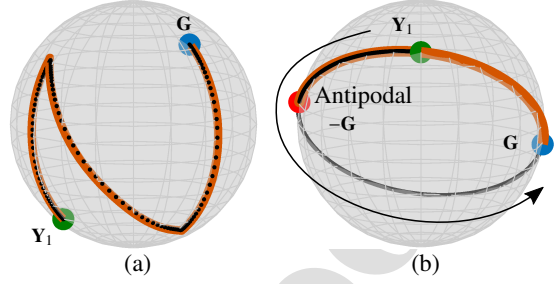


Figure 2: Results of \mathcal{G} -DMP while learning and producing trajectories that cover both south and north hemispheres. Black dashed curves denote demonstrations, while brown curves represent reproduction. Green point \mathbf{Y}_1 denotes the starting point of the trajectory, while the blue one indicates the goal \mathbf{G} . The red point illustrates the antipodal point of the goal. The figure shows \mathcal{G} -DMP while executing a trajectory that (a) does not contain an antipodal of the goal \mathbf{G} , and (b) contains an antipodal of the goal.

where the last inequality holds if $\beta_z > 0$. Therefore, $\dot{V}(\mathbf{Y}, \mathbf{Z}) \leq 0$ everywhere in the chart and vanishes only at $\mathbf{Z} = \mathbf{0}$. The LaSalle's invariance theorem [43] allows to conclude the stability of (29)–(30). \square

Remark 1. *The results of Theorem 1 hold where the logarithmic map is uniquely defined, e.g., $\mathcal{T}_{\mathbf{Y}_{l-1}}\mathcal{M}$ can be extended as much as it will not contain points conjugate to \mathbf{Y}_{l-1} [44]. For manifolds with no cut-locus, this holds everywhere. Hence, Theorem 1 is globally valid on manifolds with no cut-locus (e.g., the manifold of SPD matrices with positive definite eigenvalues [37]). However, for manifolds with cut-locus (e.g., unit m -sphere manifolds [35]), the logarithmic map $\text{Log}_{\mathbf{Y}}(\mathbf{G})$ is defined in a region that does not contain points conjugate to \mathbf{G} . For the unit m -sphere, the logarithmic map $\text{Log}_{\mathbf{Y}}(\mathbf{G})$ is uniquely defined everywhere apart from the antipodal point $-\mathbf{G}$.*

For illustration, we used the proposed \mathcal{G} -DMP to learn two trajectories; (i) the “N” shape on \mathcal{S}^2 provided in [33] (Fig. 2a), and (ii) a “C” curve with π diameter (Fig. 2b). The “N” trajectory covers both the north and south hemispheres and, as shown in [33], working on the Lie algebra will introduce large distortions. Moreover, the “N” shape is an antipodal free trajectory, such that $\mathbf{Y} = \{\mathbf{Y}_i\}_{i=1}^{T-1} \in \mathcal{S}^2 \mid |\mathbf{Y}_i \cdot \mathbf{G}| < 1$. However, the “C” curve includes the antipodal of \mathbf{G} . Figure 2a shows \mathcal{G} -DMP successfully reproducing the shape and converges to the goal (blue point). However, in (b), it fails to follow the trajectory when it encounters the antipodal of the goal (point in red). \mathcal{G} -DMP is supposed to follow the trajectory in the direction of the black arrow starting

373 from the green point. However, it follows the trajec- 411
 374 tory until the antipodal point, then returns back to reach 412
 375 the goal from the opposite direction. A possible way to 413
 376 solve this issue is to split the trajectory into segments. 414
 377 For the example in Fig. 2b, this can be done by splitting 415
 378 the trajectory into 2 segments, namely \mathbf{Y}_1 to \mathbf{Y}_2 , and \mathbf{Y}_2 416
 379 to \mathbf{G} , where \mathbf{Y}_2 is any point in the demonstration be- 417
 380 tween $-\mathbf{G}$ and $-\mathbf{Y}_1$. One can then fit 2 separate \mathcal{G} -DMP 418
 381 and smoothly merge them [19]. 419

382 4.4. \mathcal{G} -DMP on Riemannian manifold products 420

Let us define $\mathcal{Y} \in \mathcal{M}$ and $\mathcal{U} \in \mathcal{N}$ as two arbitrary 421
 trajectories from two Riemannian manifolds \mathcal{M} and \mathcal{N} , 422
 respectively. Let us call $\mathcal{H} = \{t_i, (\mathbf{Y}_i, \mathbf{U}_i)\}_{i=1}^T$ the set of 423
 data points in one demonstration. We can now define 424
 the composite \mathcal{G} -DMP as 425

$$\tau \dot{\mathbf{V}} = \alpha_z (\beta_z \text{Log}_{(\mathcal{Y}, \mathcal{U})}(\mathbf{G}_Y, \mathbf{G}_U) - \mathcal{V}) + \mathcal{F}(x), \quad (33)$$

$$\tau \dot{\mathbf{H}} = \mathcal{V}, \quad (34)$$

383 where $\mathcal{V} \in \mathcal{T}_{(\mathcal{Y}, \mathcal{U})}(\mathcal{M} \times \mathcal{N})$ and $\text{Log}_{(\mathcal{Y}, \mathcal{U})}(\mathbf{G}_Y, \mathbf{G}_U)$ is 426
 384 the logarithmic map that maps the attractors $\mathbf{G}_Y \in \mathcal{M}$ 427
 385 and $\mathbf{G}_U \in \mathcal{N}$ from the manifold composite $\mathcal{M} \times \mathcal{N}$ to 428
 386 the tangent space $\mathcal{T}_{(\mathcal{Y}, \mathcal{U})}(\mathcal{M} \times \mathcal{N})$ at each time-step. 429

387 As an illustrative example, consider the pose of the 430
 388 end-effector of a robot, which can be represented as 431
 389 the Cartesian product of the hypersphere \mathcal{S}^3 and 3D- 432
 390 Euclidean space \mathcal{R}^3 , i.e., $\mathcal{H} = \mathcal{S}^3 \times \mathcal{R}^3$. It is worth men- 433
 391 tioning that the pose of the end-effector of a robot can 434
 392 be alternatively represented as a homogeneous transfor- 435
 393 mation matrix $\mathbf{H} \in \mathcal{SE}(3)$ using the Lie group theory 436
 394 formulation [45]; however, in this work, we exploit the 437
 395 Cartesian product property of Riemannian manifolds. 438

396 **Remark 2.** The stability of manifold composites 441
 397 \mathcal{G} -DMP formulation in (33) and (34) can be straight- 442
 398 forwardly proven by applying Theorem 1 separately to 443
 399 \mathcal{M} and \mathcal{N} . 444

400 5. Validation 447

401 We validated the proposed \mathcal{G} -DMP in simulation as 448
 402 well as in real setups. More in detail, we performed the 449
 403 following evaluations: 450

- 404 • In simulation: 451

- 405 – We augmented two public datasets; 2D- 452
 406 LASA handwriting dataset [5] and 2D- 453
 407 Letters handwriting dataset [33] with data 454
 408 samples from three Riemannian manifolds 455
 409 (unit quaternion, rotation matrix, and sym- 456
 410 metric and positive definite matrix). 457

- We compared \mathcal{G} -DMP with the baseline ap- 411
 proaches [9] and [18]. 412

- Learning manipulability ellipsoids and posi- 413
 tion by learning $\mathcal{R}^2 \times \mathcal{S}_{++}^2$ with \mathcal{G} -DMP. 414

- Goal switching simulation. 415

- In real experiment: 416

- Refilling a watering can by learning $\mathcal{R}^3 \times \mathcal{S}^3 \times$ 417
 \mathcal{S}_{++}^3 with \mathcal{G} -DMP. 418

- Picking from different boxes task by learning 419
 $\mathcal{R}^3 \times \mathcal{S}_{++}^3$ with \mathcal{G} -DMP. 420

We have created one by modifying the 2D-LASA 421
 and the 2D-Letters datasets. Mainly, we extended both 422
 datasets to include \mathcal{S}^3 , $SO(3)$, and \mathcal{S}_{++}^2 along with the 423
 original \mathcal{R}^2 . The 2D-LASA handwriting dataset con- 424
 tains 30 classes of 2D Euclidean motions starting from 425
 different initial points and converging to the same goal 426
 $[0, 0]^T$. Each motion is demonstrated 7 times. A demon- 427
 stration has exactly 1000 samples and includes position, 428
 velocity, and acceleration profiles. On the other hand, 429
 the 2D-Letters handwriting dataset contains 26 letters 430
 of 2D Euclidean motions starting from different initial 431
 points and ending to different goals. Each motion is 432
 demonstrated 10 times. A demonstration has exactly 433
 200 samples and includes position, velocity, and accel- 434
 eration profiles. 435

The key idea to generate Riemannian data from Eu- 436
 clidean points is to consider each demonstration as an 437
 observation of a motion in the tangent space of a given 438
 Riemannian manifold. This allows us to use the expo- 439
 nential map to project the motion onto the manifold. 440
 In both datasets, demonstrations are in 2D (xy -plane), 441
 however, in order to create the 3D tangent space for both 442
 \mathcal{S}^3 and $SO(3)$, we added a z -axis to each demonstra- 443
 tion as an average of x - and y -axes. As a result, we obtain 444
 \mathcal{S}^3 and $SO(3)$ demonstrations for each demonstration from 445
 both datasets. 446

In order to create SPD training data profiles, we 447
 followed different strategies and used the 2D-LASA 448
 dataset to generate covariance matrix profiles and the 449
 2D-Letters dataset to generate manipulability profiles. 450
 More in detail, we first fit a GMM for each class of the 451
 2D-LASA dataset. We then used GMR to retrieve a 2×2 452
 covariance matrix profile. This covariance matrix pro- 453
 file served as SPD training data for \mathcal{G} -DMP. Instead, 454
 for the 2D-Letters dataset, we placed the base of a 3- 455
 DoF 2D-manipulator at $[0, 0]^T$, and determined the ma- 456
 nipulability profile of the manipulator while it tracks the 457
 Cartesian trajectory of each demonstration. This manip- 458
 ulability profile served as SPD training data for \mathcal{G} -DMP. 459

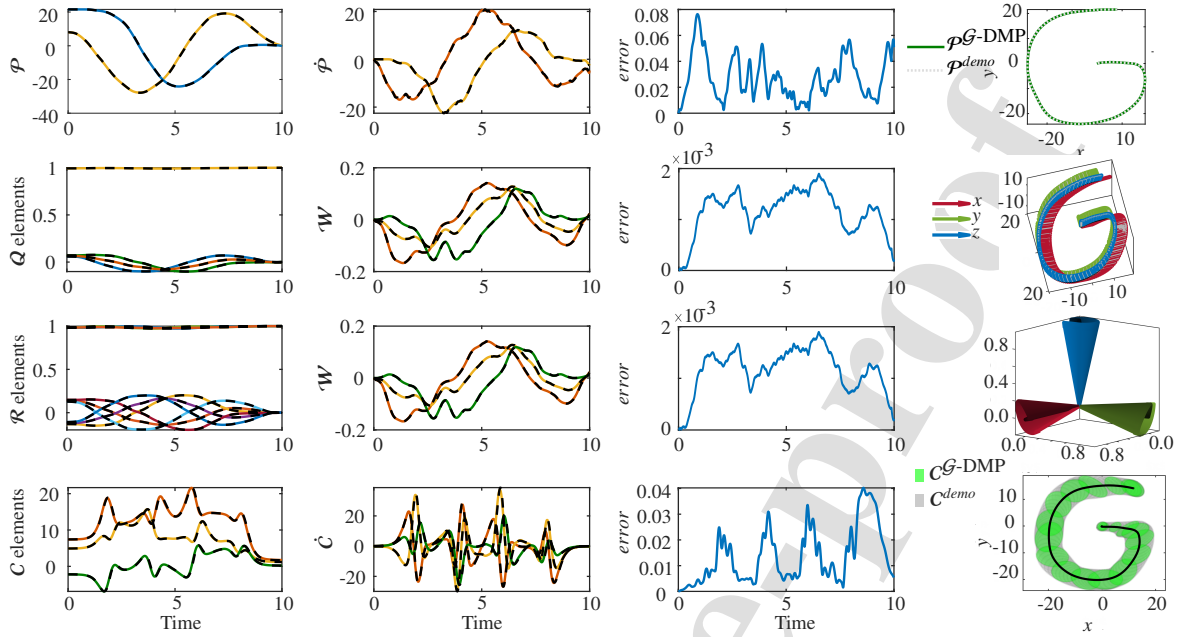


Figure 3: Illustrates the performance of \mathcal{G} -DMP when executing Riemannian LASA dataset. 1st row: Euclidean 2D trajectory, 2nd row: Unit quaternion trajectory, 3rd row: Rotation matrix trajectory, 4th row: SPD trajectory, 1st column: Trajectories from different manifolds, 2nd column: first-derivative in different manifolds, 3rd column: The distance in each manifold between the demonstration and the \mathcal{G} -DMP reproduction, 4th column: The Cartesian representation of the \mathcal{G} -DMP reproduction. In 1st and 2nd columns, dashed lines represent demonstration data while colored solid lines represent the \mathcal{G} -DMP results.

5.1. Validation using Riemannian LASA dataset

In order to validate the accuracy of the proposed unified DMP formulation, we created 4 tests in 4 different manifolds, $\mathcal{P} \in \mathcal{R}^2$, $\mathcal{Q} \in \mathcal{S}^3$, $\mathcal{R} \in SO(3)$, and $\mathcal{C} \in \mathcal{S}_{++}^2$. These are illustrated in Fig. 3 where each row corresponds to a particular manifold. The leftmost column of the figure represents the evolution of the elements of the profile over time². Dashed black lines represent the demonstration and colored lines the reproduction of \mathcal{G} -DMP. The second column corresponds to the 1st-time-derivative of the profiles in each manifold, while the 3rd column shows the error or the distance between the \mathcal{G} -DMP profile and the demonstration profile for each manifold. The last column (rightmost) shows what the profile looks like in Cartesian space. In the case of \mathcal{S}^3 , we rotate the 3D-frame of the 3D-Cartesian profile of the G-shape, while in $SO(3)$ we show the frame rotating around $[0, 0, 0]^T$. In the case of the \mathcal{S}_{++}^2 , we illustrated the covariance matrices over the 2D-Cartesian

²As SPD matrices are symmetric, and for visualization purposes, in this figure we visualize the SPD by plotting the corresponding Mandel representation.

profile of the G-shape. The results shown in this figure demonstrate the accuracy of the proposed \mathcal{G} -DMP to reproduce the desired trajectory profiles in different manifolds.

5.2. Comparison with [9]

The proposed \mathcal{G} -DMP is rigorously derived in Sec. 4.1 starting from a generic second-order dynamics evolving on a manifold. Therefore, our formulation is mathematically correct and it does not exhibit the oscillatory behaviors described in [9]. In addition to the mathematical derivation, we provide in this simulation an experimental comparison to support our claim.

More in detail, we compared our \mathcal{G} -DMP against the quaternion-based DMP proposed in³ [9]. We used the same simulated unit quaternion trajectory, where the initial and final quaternions are $\mathbf{Q}_0 = [-0.0092 \quad -0.7126 \quad 0.7015 \quad 0.0090]^T$ and $\mathbf{Q}_g = [0.8104 \quad 0.3364 \quad 0.2141 \quad 0.4293]^T$. Moreover, we used

³We thank Leonidas Koutras for sharing with us the implementation and test trajectory of their work in [9].

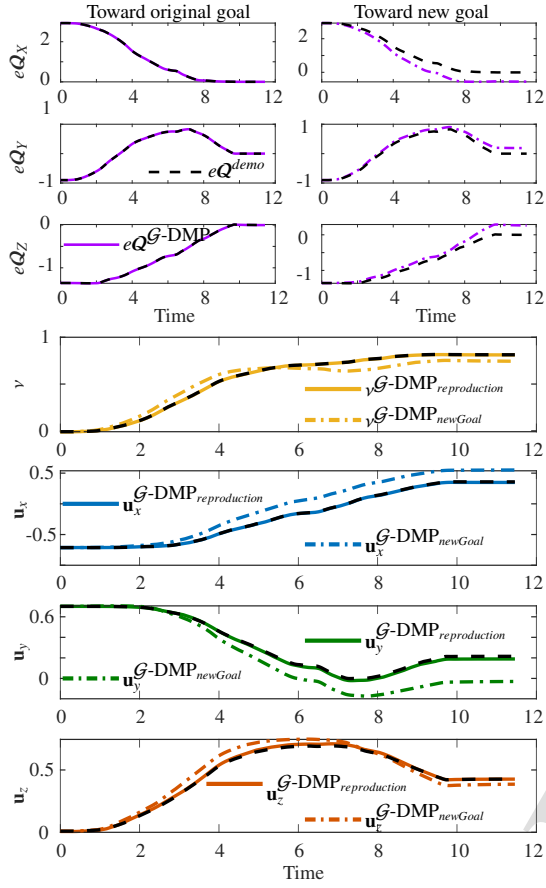


Figure 4: \mathcal{G} -DMP execution of the same unit quaternion trajectory tested in [9]. The first three rows show the error between the current unit quaternion and the goal (left) and new goal (right). The bottom four rows show the evolution of each unit quaternion element, over time, toward the original goal and the new one. Dashed black lines represent information related to the demonstration trajectory.

497 the same DMP parameters, e.g., $\alpha_z = 60$, $N = 60$,
 498 and $\alpha_x = 4.6052$. Top-left column of Fig. 4 shows
 499 the evolution of the quaternion error computed between
 500 the current (from \mathcal{G} -DMP) and goal quaternions
 501 through $e_Q = 2\text{Log}_Q(\mathbf{Q}_g)$. The top-right column shows
 502 the evolution of the error toward a new goal $\mathbf{Q}_g^{new} =$
 503 $[0.7442 \ 0.5414 \ -0.0343 \ 0.3897]^T$. The bottom 4 plots,
 504 show the evolution of the trajectories of unit quaternion
 505 elements toward the original goal and the new one. This
 506 figure shows the accuracy of the proposed \mathcal{G} -DMP to
 507 encode and execute a challenging unit quaternion trajectory.
 508 Moreover, it is clear that \mathcal{G} -DMP successfully
 509 performs a goal-switching task.

510 Figure 5 compares the accuracy of our \mathcal{G} -DMP with

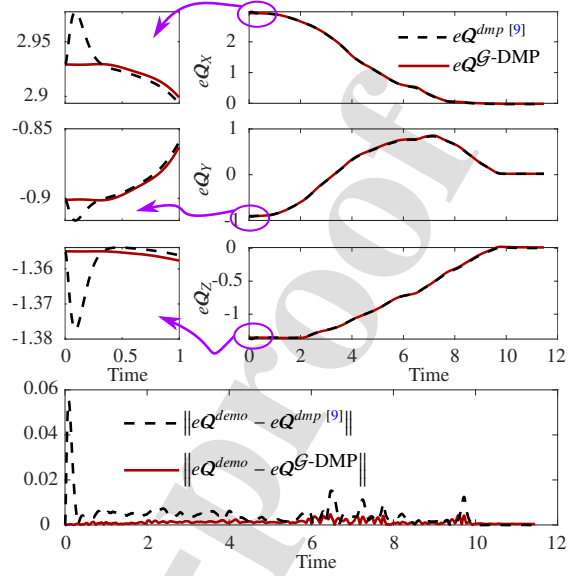


Figure 5: Comparison between the proposed \mathcal{G} -DMP and [9]. The first three rows show more stable starting using \mathcal{G} -DMP. Bottom: Compares the mean error of \mathcal{G} -DMP (in red) and [9] (dashed black lines).

511 the approach proposed in [9]. The *bottom* plot shows
 512 that the proposed \mathcal{G} -DMP is more accurate.

513 Furthermore, the computational complexity during
 514 execution, particularly in terms of step time, remains
 515 compatible with control frequencies. Specifically, the
 516 means of the computational cost exhibited by [9] and
 517 \mathcal{G} -DMP at each control cycle are 0.04 ms and 0.1 ms,
 518 respectively. We also consider a baseline approach that
 519 uses the classical DMP and performs an extra normal-
 520 ization of the output. For the baseline, the mean compu-
 521 tational cost for integrating and normalizing the output
 522 to reproduce a unit quaternion is 0.008 ms per time step.
 523 This indicates that all considered approaches can com-
 524 fortably operate at frequencies exceeding 1 kHz, ensur-
 525 ing real-time responsiveness in robotic control applica-
 526 tions.

5.3. Comparison with [18]

527 To illustrate the difference between our new formu-
 528 lation in (17)–(18) and our previous formulation
 529 described in [18], where parallel transport was em-
 530 ployed, we have conducted an experiment where both
 531 approaches executed 20 \mathcal{S}_{++}^2 trajectories of the modi-
 532 fied Riemannian LASA dataset (Sec. 5). Figure 6 shows
 533 bar plots for computational time required for both ap-
 534 proaches to learn and execute complete trajectories, and
 535

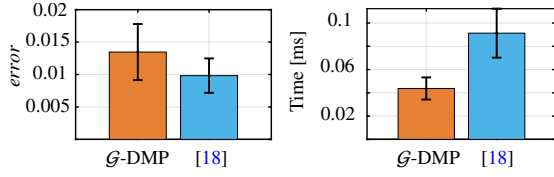


Figure 6: Comparison between the proposed \mathcal{G} -DMP and our previous approach using parallel transport [18]. Both approaches executed 20 \mathcal{S}_{++}^2 trajectories of the modified Riemannian LASA dataset. *Left*: The error distance between the demonstration and the reproduction. *Right*: The computational cost in milliseconds per control cycle.

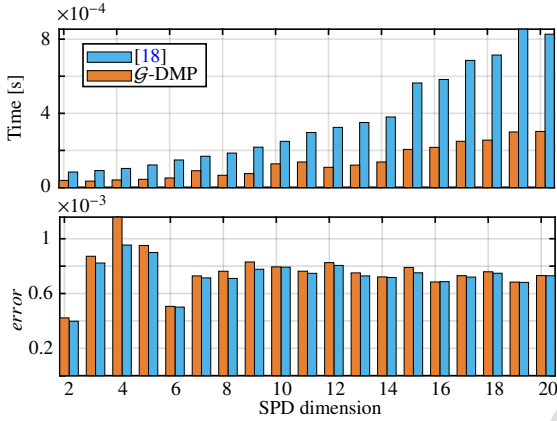


Figure 7: Comparison between the proposed \mathcal{G} -DMP and our previous approach using parallel transport [18]. Both approaches executed 19 \mathcal{S}_{++}^m trajectories, where $m = 2, \dots, 20$. *Top*: The computational cost in milliseconds per control cycle. *Bottom*: The error distance between the demonstration and the reproduction.

the log-Euclidean distance [46] between the generated SPD profiles and the ground truth demonstrations.

Results in Fig. 6 show that employing parallel transport provides slightly more accurate results, as evidenced by the reduced log-Euclidean distance from the ground truth demonstrations. However, this improvement comes at a significant computational cost, as indicated by the increased computational time required for this approach. For instance, the mean of the computational cost exhibited by [18] and \mathcal{G} -DMP at each control cycle are 0.09 ms and 0.04 ms, respectively.

In Fig. 7 we observe how this computational cost increases exponentially with the approach in [18] as problem dimensions increase. Though [18] exhibits a slight improvement in accuracy, this must be weighed against its heightened computational demands. In this example, we executed both approaches, in [18] and \mathcal{G} -DMP, over 19 SPD trajectories with dimensions ranging from \mathcal{S}_{++}^2

to \mathcal{S}_{++}^{20} , providing a comprehensive comparison.

This trade-off between accuracy and computational efficiency is an important consideration in the selection of the appropriate formulation for specific applications. For tasks where computational resources are abundant and accuracy is paramount, the parallel transport approach may be preferred. However, the new formulation offers a more efficient alternative without penalizing the accuracy for real-time applications or scenarios with limited computational resources. Finally, it is important to note that, while the approach in [18] is specifically designed for SPD matrices, our \mathcal{G} -DMP framework is applicable to any Riemannian manifold.

5.4. Learning manipulability ellipsoids

The manipulability of a robotic arm provides an analytical way to evaluate the manipulator's ability to change its end-effector pose from a certain joint configuration. Manipulability can be illustrated as an ellipsoid in 2- or 3-D Euclidean space. Mathematically, the manipulability of a robotic arm is computed from the forward kinematics

$$\dot{\mathcal{P}} = \mathbb{J}\dot{\mathcal{J}}, \quad (35)$$

that relates task velocity $\dot{\mathcal{P}} \in \mathcal{R}^m$ and the joint velocity $\dot{\mathcal{J}} \in \mathcal{R}^n$ through the Jacobian matrix $\mathbb{J} \in \mathcal{R}^{m \times n}$. By considering, in (35), only the joint velocity with unit norm, i.e., $\|\dot{\mathcal{J}}\| = \dot{\mathcal{J}}^\top \dot{\mathcal{J}} = 1$, we obtain

$$\dot{\mathcal{J}}^\top \dot{\mathcal{J}} = \dot{\mathcal{P}}^\top (\mathbb{J}^\dagger)^\top \mathbb{J}^\dagger \dot{\mathcal{P}} = \mathcal{P}^\top (\mathbb{J}\mathbb{J}^\top)^\dagger \dot{\mathcal{P}}, \quad (36)$$

which defines a point on the surface of an ellipsoid in the end-effector velocity space. The SPD matrix $\Upsilon = (\mathbb{J}\mathbb{J}^\top)^\dagger \in \mathcal{S}_{++}^m$, called manipulability ellipsoid, gives an intuition of the directions where the manipulator can move its end-effector at large/small velocities.

Here we propose to use a toy example similar to the one in [47] to evaluate our \mathcal{G} -DMP formulation while operating SPD data profiles. One demonstration $\Xi = \{t_i, \mathcal{Y}_i\}_{i=1}^T$ is obtained by performing a tracking task with a 3-DoF manipulator. Let us call \mathcal{P} the Cartesian position trajectory of the robot end-effector. The desired position trajectory $\dot{\mathcal{P}}$ is then tracked by a 5-DoF robot. The force \mathcal{F} needed to perform the tracking task is computed using the following control law originally proposed in [47]

$$\tau_d = \mathbb{J}^\top \mathcal{F} - (\mathbf{I} - \mathbb{J}^\top \bar{\mathbb{J}}) \alpha \nabla g_r(\mathcal{J}); \quad \alpha > 0, \quad (37)$$

where $\bar{\mathbb{J}}$ is the inertia-weighted pseudo-inverse of \mathbb{J} and τ_d is the desired joint torque. The cost function $g_r(\mathcal{J})$ is

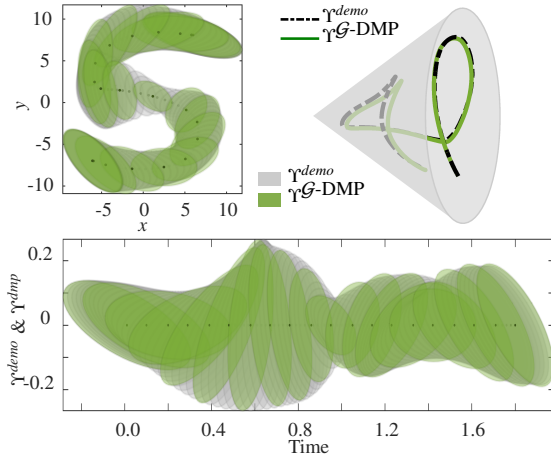


Figure 8: *Top-Left*: The Cartesian trajectory (in centimeters) executed by the 5-DoF manipulator (black dots), the demonstrated manipulability profile (gray ellipses), and the manipulability profile learned by \mathcal{G} -DMP (green ellipses), shown at different times during the execution of the task. *Top-Right*: Representation of SPD manifold (gray cone) containing the demonstrated (dashed black line) and learned (green solid line) manipulability profiles. *Bottom*: Variation of demonstrated (gray ellipses) and learned (green ellipses) manipulability profiles over time.

defined as

$$g_t(\mathcal{J}) = \log \left(\det \left(\frac{\hat{\mathbf{Y}}_t + \mathbf{Y}_{a,t}(\mathcal{J})}{2} \right) \right) - \frac{1}{2} \log \left(\det \left(\hat{\mathbf{Y}}_t \mathbf{Y}_{a,t}(\mathcal{J}) \right) \right), \quad (38)$$

where $\mathbf{Y}_{a,t}(\mathcal{J})$ are the actual and $\hat{\mathbf{Y}}_t$ the desired manipulability ellipsoids, respectively. $\hat{\mathbf{Y}}_t$ are generated using the proposed \mathcal{G} -DMP.

The results of this procedure, applied to track a 2-D S-shape Cartesian trajectory, are shown in Fig. 8. Figure 8(*top-left*) shows that the desired manipulability profile (green ellipses) smoothly and accurately follows the demonstrated manipulability profile (gray ellipses) while the 5-DoF robot was performing the tracking task. Similar results are shown in Fig. 8(*bottom*), but considering the time evolution of desired and demonstrated manipulability ellipsoids. Figure 8(*top-right*) depicts the SPD manifold (a cone) and the geodesic curve of the desired and demonstrated manipulability profiles. The \mathcal{G} -DMP successfully and accurately followed the demonstrated Cartesian trajectory along with the manipulability profile, in its composite Riemannian form $\mathcal{R}^2 \times \mathcal{S}_{++}^2$, and converged to the goal.

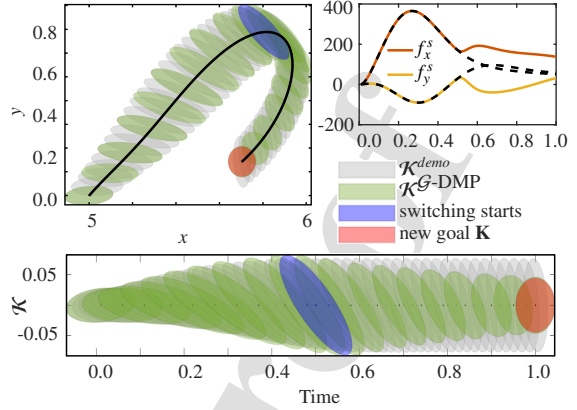


Figure 9: \mathcal{G} -DMP adapts the stiffness profile to a new goal using the mechanism of goal switching (28). Gray ellipsoids represent the demonstrated stiffness profile, green ones are the result of \mathcal{G} -DMP, the blue one indicates the instant where goal switching occurred, and the red one denotes the new goal ellipsoid. *Top-Left*: The evolution of \mathcal{G} -DMP over a Cartesian trajectory. *Bottom*: The evolution of \mathcal{G} -DMP over time. *Top-Right*: The evolution of the spring forces while tracking the Cartesian trajectory.

5.5. Goal switching

In order to evaluate the proposed \mathcal{G} -DMP formulation characteristics under goal switching, we used it to drive an virtual-Mass Spring-Damper (MSD), with a designed variable stiffness profile, along a specific Cartesian trajectory. The variable stiffness profile is designed, such that, it starts with, horizontally-aligned stiffness ellipsoid, $[622.9934 \ 39.9577; 39.9577 \ 79.5444]$, then we rotated it gradually 90° , through $\mathbf{R}^\top \mathcal{K} \mathbf{R}$ (\mathbf{R} is a rotation matrix), until it ends up with, vertically-aligned stiffness ellipsoid, $[79.5444 \ -39.9577; -39.9577 \ 588.2443]$. This stiffness profile $\mathcal{K} \in \mathcal{S}_{++}^2$ is our demonstration, the gray ellipsoids in Fig. 9(*top-left*), along with the Cartesian trajectory $\mathcal{P} \in \mathcal{R}^2$, solid black curve. In this simulation, \mathcal{G} -DMP encodes the composite Riemannian manifolds $\mathcal{R}^2 \times \mathcal{S}_{++}^2$.

During the execution, we estimated the spring forces \mathbf{f}^s while tracking the Cartesian trajectory. The \mathcal{G} -DMP reproduction, in the first execution, has been successfully converged to the original goal, dashed lines in Fig. 10(*bottom*). In the second execution, we switched to a new stiffness goal $[200 \ 0; 0 \ 200]$, red ellipsoid in Fig. 9, at the middle of the execution. From Fig. 10(*top*), we can see the error between \mathcal{G} -DMP stiffness result, at each time step, and the new stiffness goal converges to zero (the solid red line), which indicates that the \mathcal{G} -DMP converges accurately to the new stiffness goal.

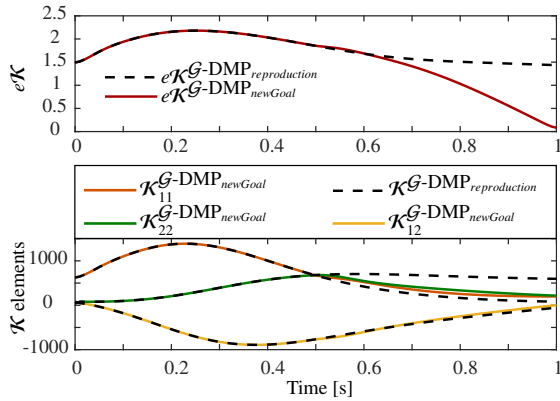


Figure 10: *Top*: The Log-Euclidean distance between \mathcal{G} -DMP evolution and the goal in both cases; reproduction (dashed black lines), adaptation using goal switching (red solid line). *Bottom*: The element of stiffness profile in reproduction (dashed black lines) and adaptation using goal switching (colored solid lines).

5.6. Robot experiments

We evaluated the proposed approach on a 7 DoF Franka Emika Panda robot with two experiments, namely picking from different boxes and refilling a watering can. In order to perform these tasks, the robot had to continuously modulate its position, orientation, stiffness, and/or manipulability. In real settings, orientation trajectories are often collected from demonstrations with a real robot. This requires a preprocessing step to extract unit quaternions from a trajectory of rotation matrices. The step is needed because the robot's forward kinematics is typically expressed as a homogeneous transformation matrix [48]. Numerical approaches to continuously compute quaternions from rotation matrices may return a quaternion at time t and its antipodal at $t + 1$, since antipodal quaternions represent the same rotation. The resulting discontinuity can be avoided by checking that the dot product $\mathbf{q}_t \cdot \mathbf{q}_{t+1} > 0$ and replacing \mathbf{q}_{t+1} with $-\mathbf{q}_{t+1}$ otherwise.

5.6.1. Refilling a watering can

In this experiment, the robot had to refill a watering can by immersing it in a tray full of water (see Fig. 11). To perform the task, the robot was controlled using the Cartesian impedance control law

$$\begin{aligned} \mathcal{F}_p &= \mathcal{K}_p (\mathcal{P}^{dmp} - \mathcal{P}) + \mathcal{D}_p (\dot{\mathcal{P}}^{dmp} - \dot{\mathcal{P}}), \\ \mathcal{F}_o &= \mathcal{K}_o \text{Log}_Q (\mathcal{Q}^{dmp}) + \mathcal{D}_o (\mathcal{W}^{dmp} - \mathcal{W}), \end{aligned} \quad (39)$$

where the subscript p indicates position and o orientation. The measured end-effector position and orienta-

tion (unit quaternion) are indicated by \mathcal{P} and \mathcal{Q} respectively, and the corresponding linear and angular velocities are $\dot{\mathcal{P}}$ and \mathcal{W} . The desired trajectories \mathcal{P}^{dmp} and \mathcal{Q}^{dmp} , as well as the variable stiffness matrix \mathcal{K}_p and the desired velocities $(\dot{\mathcal{P}}^{dmp}$ and $\mathcal{W}^{dmp})$, were generated with the proposed \mathcal{G} -DMP. The orientation stiffness was kept constant at $\mathcal{K}_o = 150 \text{ INm/rad}$. The damping matrices \mathcal{D}_p and \mathcal{D}_o were computed from the respective stiffness matrices using the double diagonalization approach [49]. The robot was controlled at 1 KHz using the joint torques

$$\boldsymbol{\tau}_d = \mathbb{J}^T \begin{bmatrix} \mathcal{F}_p \\ \mathcal{F}_o \end{bmatrix}, \quad (40)$$

where \mathbb{J}^T is the transpose of the manipulator Jacobian and the Cartesian forces \mathcal{F}_p and \mathcal{F}_o are defined as in (39).

Desired position, velocity, and stiffness profiles were learned using the proposed \mathcal{G} -DMP. In order to estimate a variable stiffness profile, we collected 5 kinesthetic demonstrations containing end-effector positions, velocities, accelerations, and sensed forces. These data were used through the interaction model proposed in [16] to estimate the variable stiffness profile shown in Fig. 11 (bottom). Positions and unit quaternion trajectories were learned from a single demonstration, obtained by averaging the 5 used to obtain the stiffness profile.

The results in Fig. 11 show that the proposed \mathcal{G} -DMP formulation is capable of learning complex trajectories evolving on composite Riemannian manifolds $\mathcal{R}^3 \times \mathcal{S}^3 \times \mathcal{S}_{++}^3$ while fulfilling the underlying geometric constraints, *i.e.*, unit norm in variable orientation and symmetry and positive definiteness in variable stiffness profiles.

5.6.2. Pick from different boxes

In this experiment, the robot had to enter 3 boxes placed at different locations, mimicking a pick from each of the boxes (see Fig. 12). The experiment was designed to show that geometry-aware DMPs can *i)* effectively encode manipulability profiles and *ii)* change the goal after the learning.

We provided a kinesthetic demonstration to make the robot enter box 1 while collecting end-effector position and joint trajectories. As detailed in Sec. 5.4, collected trajectories were used to learn position and manipulability profiles using geometry-aware DMPs. At run time, the robot was controlled using the control law (37) to track the DMP position as main task and to exploit its redundant DoF to follow the desired manipulability profile. As shown in Fig. 12 (top), the robot followed ac-

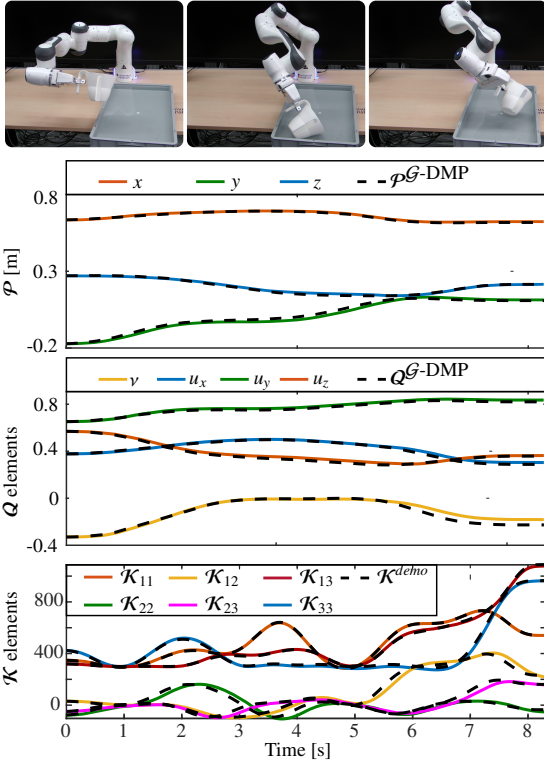


Figure 11: Results for the refill of a watering can experiment. *Top*: The robot correctly performs the task. *Bottom*: Position, orientation, and stiffness profiles.

674 curately both position and manipulability profiles and
675 successfully entered box 1.

676 In order to experimentally verify the generalization
677 capabilities of geometry-aware DMPs, we repeated the
678 experiment by entering two boxes placed at different loca-
679 tions wrt box 1. To measure the new goal, we manu-
680 ally placed the robot inside the boxes and stored its
681 end-effector position. As shown in Fig. 12 (middle)–
682 (bottom), the robot reached the new position goals in-
683 side box 2 and 3. As already mentioned, the manipula-
684 bility profile was tracked in the null-space of the posi-
685 tion task, which introduces an error between the planned
686 and executed manipulability profiles. However, in this
687 task, null-space tracking was sufficient to preserve a
688 joint configuration that let the robot enter boxes 2 and
689 3 without collision.

690 Overall, the results in Fig. 12 show that the proposed
691 \mathcal{G} -DMP formulation is capable of learning complex tra-
692 jectories evolving on the composite Riemannian mani-
693 fold $\mathcal{R}^3 \times \mathcal{S}_{++}^3$ while fulfilling the underlying geometric
694 constraints, *i.e.*, symmetry and positive definiteness in

695 variable manipulability profiles.

696 6. Conclusion

697 In this paper, we have exploited Riemannian geom-
698 etry to derive a new formulation of DMP that is capa-
699 ble of learning and reproducing robot skills evolving
700 on any Riemannian manifold. Our new formulation,
701 Geometry-aware DMP (\mathcal{G} -DMP), is manifold indepen-
702 dent and allows us to treat data belonging to different
703 manifolds in a unified manner. It also preserves the
704 underlying geometric constraints during both learning
705 and reproduction without pre- or post-processing of the
706 data. Moreover, it preserves the properties of the clas-
707 sical DMP formulation such as convergence to a given
708 target and the possibility to change the target at run-time
709 (goal switching).

710 \mathcal{G} -DMP has been extensively validated through mul-
711 tiple simulation examples and two experiments on a real
712 robotic manipulator. For simulation, we augmented two
713 Euclidean datasets (2D-Letters and LASA handwriting)
714 with data samples from three Riemannian manifolds
715 (\mathcal{S}^3 , $SO(3)$, and \mathcal{S}_{++}^2). We showed that \mathcal{G} -DMP can ac-
716 curately learn profiles evolving on such manifolds while
717 converging to a (possibly changing) goal. Moreover, a
718 comparison with a baseline approach was conducted on
719 a unit quaternion trajectory. In this case, \mathcal{G} -DMP shows
720 improvement by avoiding slight jumps at the beginning
721 of the trajectories. Finally, real experiments show the ef-
722 fectiveness of \mathcal{G} -DMP in encoding data from manifolds
723 such as orientation, and SPD matrices.

724 In the future, we propose to integrate our approach
725 with iterative learning algorithms—for example itera-
726 tive learning control—in order to adapt to different situ-
727 ations and perform more complex tasks such as physical
728 interaction control. Moreover, extending exploration-
729 based learning methods to Riemannian manifolds is an
730 open research problem. These methods are crucial when
731 a robot needs to significantly adapt its behavior to a new
732 situation by considering the data directly on its corre-
733 sponding manifold. This will allow us to successfully
734 exploit \mathcal{G} -DMPs in a large diversity of task situations.

735 Appendix A. Characterization of Used Manifolds

736 Appendix A.1. The SPD manifold \mathcal{S}_{++}^m

737 As early mentioned, SPD matrices is important in
738 robotics as it encapsulate different types of data. The
739 space \mathcal{S}_{++}^m is defined as the space of $m \times m$ Symmet-
740 ric Positive Definite matrices. This space is not closed
741 under scalar product and addition [37], thus, we cannot

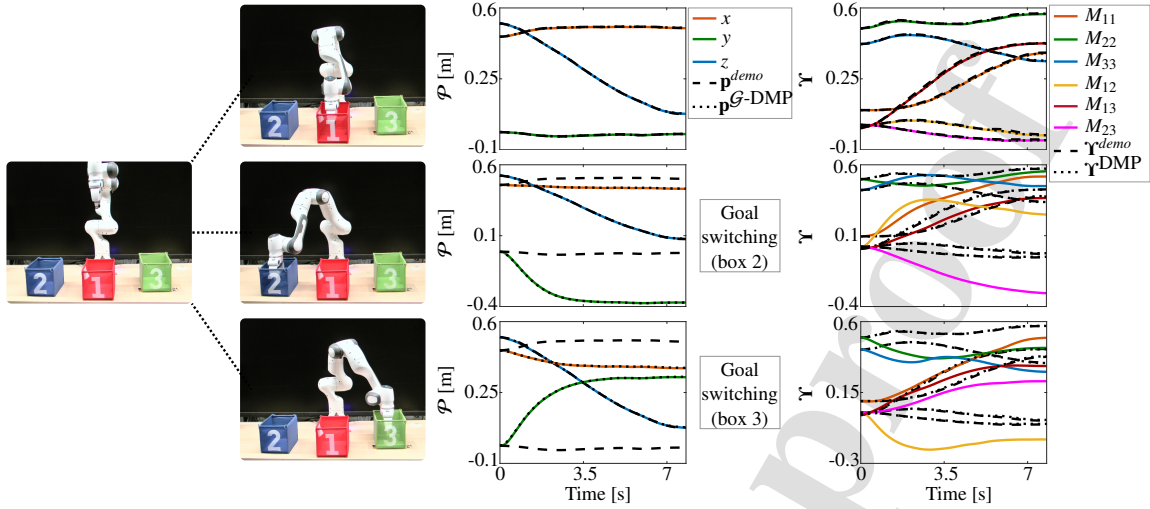


Figure 12: Results for the pick from different boxes experiment. *Top*: Picking from the demonstrated box 1. *Middle*: Goal switching is used to pick from a new box 2. *Bottom*: Goal switching is used to pick from a new box 3. In the 3 cases, manipulability is controlled in the null-space of the position task to maintain a certain joint configuration during the motion.

use classical Euclidean arithmetic operators to manipulate these matrices. Alternatively, we can equip SPD matrices with a Riemannian metric in order to form a Riemannian manifold [37].

Note that the space S_{++}^m can be represented as the interior of a convex cone embedded in its tangent space of symmetric $m \times m$ matrices \mathcal{SYM}^m .

For $\mathbf{Q}, \mathbf{U} \in S_{++}^m$ and $\mathbf{v} \in \mathcal{T}_{\mathbf{U}}S_{++}^m$, the logarithmic and exponential maps (8) and (9) can be defined as in [37]

$$\mathbf{v} = \text{Log}_{\mathbf{U}}(\mathbf{Q}) = \mathbf{U}^{\frac{1}{2}} \text{logm}(\mathbf{U}^{-\frac{1}{2}} \mathbf{Q} \mathbf{U}^{-\frac{1}{2}}) \mathbf{U}^{\frac{1}{2}}, \quad (\text{A.1})$$

$$\mathbf{Q} = \text{Exp}_{\mathbf{U}}(\mathbf{v}) = \mathbf{U}^{\frac{1}{2}} \text{expm}(\mathbf{U}^{-\frac{1}{2}} \mathbf{v} \mathbf{U}^{-\frac{1}{2}}) \mathbf{U}^{\frac{1}{2}}, \quad (\text{A.2})$$

where $\text{logm}(\cdot)$ and $\text{expm}(\cdot)$ are the matrix logarithm and exponential functions.

Appendix A.2. The unit m -sphere manifold S^m

S^m is a topological space embedded in \mathcal{R}^{m+1} Cartesian space, where $S^m = \{\mathbf{X} \in \mathcal{R}^{m+1} : \|\mathbf{X}\| = 1\}$. For $\mathbf{Q}, \mathbf{U} \in S^m$ and $\mathbf{v}, \mathbf{r} \in \mathcal{T}_{\mathbf{U}}S^m$ then, the logarithmic and exponential maps (9) and (8) are defined as in [50]

$$\mathbf{v} = \text{Log}_{\mathbf{U}}(\mathbf{Q}) = \frac{\mathbf{Q} - (\mathbf{U}^{\top} \mathbf{Q} \mathbf{U})}{\|\mathbf{Q} - (\mathbf{U}^{\top} \mathbf{Q} \mathbf{U})\|} d(\mathbf{U}, \mathbf{Q}), \quad (\text{A.3})$$

$$\mathbf{Q} = \text{Exp}_{\mathbf{U}}(\mathbf{v}) = \mathbf{U} \cos(\|\mathbf{v}\|) + \frac{\mathbf{v}}{\|\mathbf{v}\|} \sin(\|\mathbf{v}\|), \quad (\text{A.4})$$

where $d(\mathbf{U}, \mathbf{Q}) \equiv \arccos(\mathbf{Q}^{\top} \mathbf{U})$ defines the geodesic distance between \mathbf{Q} and \mathbf{U} .

Appendix A.3. The unit quaternions group S^3

One way to describe the robot's end-effector orientation, in 3D-space, is to use unit quaternion representation. For $\mathbf{Q}, \mathbf{U} \in S^3$ and $\mathbf{v}, \mathbf{r} \in \mathcal{T}_{\mathbf{U}}S^3 \equiv \mathcal{R}^3$, where S^3 is a unit sphere in \mathcal{R}^4 , $\mathbf{Q} = v_q + \mathbf{u}_q$, $v_q \in \mathcal{R}$, and $\mathbf{u}_q \in \mathcal{R}^3$. The logarithmic and exponential maps (8) and (9) are

$$\begin{aligned} \mathbf{v} &= \text{Log}_{\mathbf{U}}(\mathbf{Q}) = \text{Log}(\mathbf{Q} * \bar{\mathbf{U}}) \\ &= \begin{cases} \arccos(v) \frac{\mathbf{u}}{\|\mathbf{u}\|}, & \mathbf{u} \neq \mathbf{0} \\ [0 \ 0 \ 0]^{\top}, & \text{otherwise.} \end{cases} \end{aligned} \quad (\text{A.5})$$

$$\begin{aligned} \mathbf{Q} &= \text{Exp}_{\mathbf{U}}(\mathbf{v}) \\ &= \begin{cases} [\cos(\|\mathbf{v}\|) + \sin(\|\mathbf{v}\|) \frac{\mathbf{v}}{\|\mathbf{v}\|}] * \mathbf{U}, & \mathbf{v} \neq \mathbf{0} \\ [1 + [0 \ 0 \ 0]^{\top}] * \mathbf{U}, & \text{otherwise.} \end{cases} \end{aligned} \quad (\text{A.6})$$

where $\mathbf{Q} * \bar{\mathbf{U}} = v + \mathbf{u} \in S^3$, and $\mathbf{v} \in \mathcal{R}^3$ is treated as a quaternion with $v = 0$.

Appendix A.4. The special orthogonal group $SO(m)$

$SO(m)$ is a subgroup of the orthogonal group $O(m)$ where its determinant is 1. Let us define $\mathbf{R}_1, \mathbf{R}_2 \in SO(m)$ and $\mathbf{v} \in \mathcal{T}_{\mathbf{R}_1}SO(m)$, then the logarithmic and exponential maps (9) and (8) are defined as in [50]

$$\mathbf{v} = \text{Log}_{\mathbf{R}_1}(\mathbf{R}_2) = \text{logm}(\mathbf{R}_1^{\top} \mathbf{R}_2), \quad (\text{A.7})$$

$$\mathbf{R}_2 = \text{Exp}_{\mathbf{R}_1}(\mathbf{v}) = \text{expm}(\mathbf{v}) \mathbf{R}_1. \quad (\text{A.8})$$

Appendix A.5. The rotation group $SO(3)$

Traditionally, orientations, in 3D-space, were represented through rotation matrices in $SO(3) = \{\mathbf{R} \in \mathcal{R}^{3 \times 3} : |\mathbf{R}| = 1, \mathbf{R}^T \mathbf{R} = \mathbf{R} \mathbf{R}^T = \mathbf{I}\}$ which are widely used in robotics. Let us define $\mathbf{R}_1, \mathbf{R}_2 \in SO(3)$ and $\mathbf{v} \in \mathcal{T}_{\mathbf{R}_1} SO(3)$, then (8) will be [51]

$$\begin{aligned} \mathbf{v} &= \text{Log}_{\mathbf{R}_1}(\mathbf{R}_2) = \text{Log}(\mathbf{R}_2 \mathbf{R}_1^T) = \text{Log}(\mathbf{R}) \\ &= \begin{cases} [0, 0, 0]^T, & \mathbf{R} = \mathbf{I} \\ \boldsymbol{\omega} = \theta \mathbf{n}, & \text{otherwise,} \end{cases} \end{aligned} \quad (\text{A.9})$$

where

$$\theta = \arccos\left(\frac{\text{trace}(\mathbf{R}) - 1}{2}\right), \quad \mathbf{n} = \frac{1}{2 \sin(\theta)} \begin{bmatrix} r_{32} - r_{23} \\ r_{13} - r_{31} \\ r_{21} - r_{12} \end{bmatrix}$$

and (9) will be

$$\begin{aligned} \mathbf{R}_2 &= \text{Exp}_{\mathbf{R}_1}([\mathbf{v}]_{\times}) \\ &= \left(\mathbf{I} + \sin(\theta) \frac{[\mathbf{v}]_{\times}}{\|\mathbf{v}\|} + (1 - \cos(\theta)) \frac{[\mathbf{v}]_{\times}^2}{\|\mathbf{v}\|^2} \right) \mathbf{R}_1, \end{aligned} \quad (\text{A.10})$$

Note that the mappings in (A.5)–(A.6) and in (A.9)–(A.10) are computed using Lie group theory as unit quaternions and rotation matrices form a Lie group [45]. In particular, the mappings are based on the tangent space placed at the identity element (the so-called Lie algebra), and the product operations are used to parallel transport vectors from the Lie algebra to the tangent space placed at a different point (\mathbf{U} or \mathbf{R}_1). We used the term Riemannian through the paper since every Lie group equipped with a Riemannian metric is a Riemannian manifold, but not vice versa.

Acknowledgements

This work is supported in part by Basque Government (ELKARTEK) projects Proflow KK-2022/00024 and HELDU KK-2023/00055, in part by the European Union project INVERSE (GA No. 101136067), and in part by CHIST-ERA project IPALM (Academy of Finland decision 326304). Real experiments were conducted at the Department of Computer Science, University of Innsbruck, Austria.

References

- [1] S. Schaal, Is imitation learning the route to humanoid robots?, *Trends in Cognitive Sciences* 3 (6) (1999) 233–242.
- [2] A. Billard, S. Calinon, R. Dillmann, *Learning from Humans*, 2016, pp. 1995–2014.

- [3] H. Ravichandar, A. S. Polydoros, S. Chernova, A. Billard, Recent advances in robot learning from demonstration, *Annual Review of Control, Robotics, and Autonomous Systems* 3 (1) (2020) 297–330.
- [4] A. J. Ijspeert, J. Nakanishi, H. Hoffmann, P. Pastor, S. Schaal, Dynamical movement primitives: learning attractor models for motor behaviors, *Neural Computation* 25 (2) (2013) 328–373.
- [5] S. M. Khansari-Zadeh, A. Billard, Learning stable non-linear dynamical systems with gaussian mixture models, *IEEE Transactions on Robotics* 27 (5) (2011) 943–957.
- [6] S. M. Khansari-Zadeh, A. Billard, Learning control Lyapunov function to ensure stability of dynamical system-based robot reaching motions, *Robotics and Autonomous Systems* 62 (6) (2014) 752–765.
- [7] A. J. Ijspeert, J. Nakanishi, S. Schaal, Learning rhythmic movements by demonstration using nonlinear oscillators, in: *IEEE/RSJ International Conference on Intelligent Robots and Systems, Lausanne, Switzerland, 2002*, pp. 958–963.
- [8] A. Ude, B. Nemeč, T. Petrić, J. Morimoto, Orientation in cartesian space dynamic movement primitives, in: *IEEE International Conference on Robotics and Automation, Hong Kong, China, 2014*, pp. 2997–3004.
- [9] L. Koutras, Z. Doulergi, A correct formulation for the orientation dynamic movement primitives for robot control in the cartesian space, in: *Conference on Robot Learning, Osaka, Japan, 2020*, pp. 293–302.
- [10] Y. Huang, F. J. Abu-Dakka, J. Silvério, D. G. Caldwell, Toward orientation learning and adaptation in cartesian space, *IEEE Transactions on Robotics* 37 (1) (2020) 82–98.
- [11] S. Traversaro, S. Brossette, A. Escande, F. Nori, Identification of fully physical consistent inertial parameters using optimization on manifolds, in: *IEEE/RSJ International Conference on Intelligent Robots and Systems, Daejeon, Korea, 2016*, pp. 5446–5451.
- [12] T. Yoshikawa, Manipulability of robotic mechanisms, *The International Journal of Robotics Research* 4 (2) (1985) 3–9.
- [13] N. Jaquier, L. Rozo, D. G. Caldwell, S. Calinon, Geometry-aware manipulability learning, tracking, and transfer, *The International Journal of Robotics Research* 40 (2-3) (2021) 624–650.
- [14] F. J. Abu-Dakka, Y. Huang, J. Silvério, V. Kyrki, A probabilistic framework for learning geometry-based robot manipulation skills, *Robotics and Autonomous Systems* 141 (2021) 103761.
- [15] R. Ikeura, H. Inooka, Variable impedance control of a robot for cooperation with a human, in: *IEEE International Conference on Robotics and Automation, Nagoya, Japan, 1995*, pp. 3097–3102.
- [16] F. J. Abu-Dakka, L. Rozo, D. G. Caldwell, Force-based variable impedance learning for robotic manipulation, *Robotics and Autonomous Systems* 109 (2018) 156–167.
- [17] F. J. Abu-Dakka, B. Nemeč, J. A. Jørgensen, T. R. Savarimuthu, N. Krüger, A. Ude, Adaptation of manipulation skills in physical contact with the environment to reference force profiles, *Autonomous Robots* 39 (2) (2015) 199–217.
- [18] F. J. Abu-Dakka, V. Kyrki, Geometry-aware dynamic movement primitives, in: *IEEE International Conference on Robotics and Automation, Paris, France, 2020*, pp. 4421–4426.
- [19] M. Saveriano, F. Franzel, D. Lee, Merging position and orientation motion primitives, in: *IEEE International Conference on Robotics and Automation, Montreal, QC, Canada, 2019*, pp. 7041–7047.
- [20] M. Saveriano, F. J. Abu-Dakka, A. Kramberger, L. Peternel, Dynamic movement primitives in robotics: A tutorial survey, *The International Journal of Robotics Research* 42 (13) (2023) 1133–1184.
- [21] A. Paraschos, C. Daniel, J. R. Peters, G. Neumann, Probabilis-

- 870 tic movement primitives, in: *Advances in Neural Information* 935
 871 *Processing Systems*, Nevada, USA, 2013, pp. 2616–2624. 936
- 872 [22] S. Calinon, D. Bruno, D. G. Caldwell, A task-parameterized 937
 873 probabilistic model with minimal intervention control, in: *IEEE* 938
 874 *International Conference on Robotics and Automation*, Hong 939
 875 Kong, China, 2014, pp. 3339–3344. 940
- 876 [23] Y. Huang, L. Rozo, J. Silvério, D. G. Caldwell, Kernelized 941
 877 movement primitives, *The International Journal of Robotics Re-* 942
 878 *search* 38 (7) (2019) 833–852. 943
- 879 [24] P. Pastor, H. Hoffmann, T. Asfour, S. Schaal, Learning and gen- 944
 880 eralization of motor skills by learning from demonstration, in: 945
 881 *IEEE International Conference on Robotics and Automation*, 946
 882 Kobe, Japan, 2009, pp. 763–768. 947
- 883 [25] J. Silvério, L. Rozo, S. Calinon, D. G. Caldwell, Learning 948
 884 bimanual end-effector poses from demonstrations using task- 949
 885 parameterized dynamical systems, in: *IEEE/RSJ International* 950
 886 *Conference on Intelligent Robots and Systems*, Hamburg, Ger- 951
 887 many, 2015, pp. 464–470. 952
- 888 [26] F. J. Abu-Dakka, M. Saveriano, L. Peternel, Periodic dmp for- 953
 889 mulation for quaternion trajectories, in: *IEEE International Con-* 954
 890 *ference of Advanced Robotics*, Ljubljana, Slovenia, 2021, pp. 955
 891 658–663. 956
- 892 [27] P.-Y. Gousenbourger, E. Massart, P.-A. Absil, Data fitting on 957
 893 manifolds with composite bézier-like curves and blended cubic 958
 894 splines, *Journal of Mathematical Imaging and Vision* 61 (5) 959
 895 (2019) 645–671. 960
- 896 [28] S. Kim, R. Haschke, H. Ritter, Gaussian mixture model for 3- 961
 897 dof orientations, *Robotics and Autonomous Systems* 87 (2017) 962
 898 28–37. 963
- 899 [29] M. J. Zeestraten, I. Havoutis, J. Silvério, S. Calinon, D. G. 964
 900 Caldwell, An approach for imitation learning on riemannian 965
 901 manifolds, *IEEE Robotics and Automation Letters* 2 (3) (2017) 966
 902 1240–1247. 967
- 903 [30] L. Dodero, H. Q. Minh, M. San Biagio, V. Murino, D. Sona, 968
 904 Kernel-based classification for brain connectivity graphs on the 969
 905 riemannian manifold of positive definite matrices, in: *IEEE In-* 970
 906 *ternational Symposium on Biomedical Imaging*, Brooklyn, NY, 971
 907 USA, 2015, pp. 42–45. 972
- 908 [31] S. Herath, M. Harandi, F. Porikli, Learning an invariant hilbert 973
 909 space for domain adaptation, in: *IEEE Conference on Computer* 974
 910 *Vision and Pattern Recognition*, Honolulu, Hawaii, 2017, pp. 975
 911 3845–3854.
- 912 [32] D. C. Alexander, C. Pierpaoli, P. J. Basser, J. C. Gee, Spatial 976
 913 transformations of diffusion tensor magnetic resonance images, 977
 914 *IEEE Transactions on Medical Imaging* 20 (11) (2001) 1131– 978
 915 1139. 979
- 916 [33] S. Calinon, Gaussians on Riemannian manifolds: Applications 980
 917 for robot learning and adaptive control, *IEEE Robotics and Au-* 981
 918 *tomation Magazine* 27 (2) (2020) 33–45. 982
- 919 [34] N. Jaquier, S. Calinon, Gaussian mixture regression on sym- 983
 920 metric positive definite matrices manifolds: Application to wrist 984
 921 motion estimation with semg, in: *IEEE/RSJ International Con-* 985
 922 *ference on Intelligent Robots and Systems*, Vancouver, Canada, 986
 923 2017, pp. 59–64. 987
- 924 [35] X. Pennec, Intrinsic statistics on riemannian manifolds: Basic 988
 925 tools for geometric measurements, *Journal of Mathematical* 989
 926 *Imaging and Vision* 25 (1) (2006) 127–154. 990
- 927 [36] P.-A. Absil, R. Mahony, R. Sepulchre, *Optimization algorithms* 991
 928 *on matrix manifolds*, Princeton University Press, 2009. 992
- 929 [37] X. Pennec, P. Fillard, N. Ayache, A riemannian framework 993
 930 for tensor computing, *International Journal of Computer Vision* 994
 931 66 (1) (2006) 41–66. 995
- 932 [38] M. Fréchet, Les éléments aléatoires de nature quelconque dans 996
 933 un espace distancié, in: *Annales de l’institut Henri Poincaré*, 997
 934 Vol. 10, 1948, pp. 215–310. 998
- [39] S. Fiori, I. Cervigni, M. Ippoliti, C. Menotta, Synthetic non- 999
 linear second-order oscillators on riemannian manifolds and 1000
 their numerical simulation, *Discrete and Continuous Dynamical* 1001
Systems-B 27 (3) (2022) 1227–1262. 1002
- [40] N. Boumal, P.-A. Absil, A discrete regression method on man- 1003
 ifolds and its application to data on $so(n)$, *IFAC Proceedings* 1004
Volumes 44 (1) (2011) 2284–2289, 18th IFAC World Congress. 1005
- [41] L. Markus, Asymptotically autonomous differential systems, in: 1006
 S. Lefschetz (Ed.), *Contributions to the Theory of Nonlinear Oscil-* 1007
lations III, Princeton University Press, 1956, pp. 17–30. 1008
- [42] S. Fiori, Manifold calculus in system theory and control- 1009
 fundamentals and first-order systems, *Symmetry* 13 (11) (2021). 1010
- [43] J. Slotine, W. Li, *Applied nonlinear control*, Prentice-Hall En- 1011
 glewood Cliffs, 1991. 1012
- [44] F. Pait, D. Colón, Some properties of the riemannian distance 1013
 function and the position vector x , with applications to the con- 1014
 struction of Lyapunov functions, in: *IEEE Conference on Deci-* 1015
sion and Control, Atlanta, GA, USA, 2010, pp. 6277–6280. 1016
- [45] J. Sola, J. Deray, D. Atchuthan, A micro lie theory for state es- 1017
 timation in robotics, *arXiv preprint arXiv:1812.01537* (2018). 1018
- [46] S. Jayasumana, R. Hartley, M. Salzmann, H. Li, M. Harandi, 1019
 Kernel methods on riemannian manifolds with gaussian rbf ker- 1020
 nels, *IEEE Transactions on Pattern Analysis and Machine Intel-* 1021
ligence 37 (12) (2015) 2464–2477. 1022
- [47] L. Rozo, N. Jaquier, S. Calinon, D. G. Caldwell, Learning ma- 1023
 nipulability ellipsoids for task compatibility in robot manipu- 1024
 lation, in: *IEEE/RSJ International Conference on Intelligent* 1025
Robots and Systems, Vancouver, Canada, 2017, pp. 3183–3189. 1026
- [48] B. Siciliano, L. Sciavicco, L. Villani, G. Oriolo, *Robotics: Mod-* 1027
elling, Planning and Control, Springer, 2009. 1028
- [49] A. Albu-Schaffer, C. Ott, U. Frese, G. Hirzinger, Cartesian 1029
 impedance control of redundant robots: Recent results with the 1030
 dlr-light-weight-arms, in: *IEEE International Conference on* 1031
Robotics and Automation, Taipei, Taiwan, 2003, pp. 3704– 1032
 3709. 1033
- [50] Q. Rentmeesters, A gradient method for geodesic data fitting on 1034
 some symmetric riemannian manifolds, in: *IEEE Conference* 1035
on Decision and Control and European Control Conference, Or- 1036
 lando, FL, USA, 2011, pp. 7141–7146. 1037
- [51] R. M. Murray, Z. Li, S. S. Sastry, *A mathematical introduction* 1038
to robotic manipulation, CRC press, 2017. 1039

Fares J. Abu-Dakka received his B.Sc. degree in Mechanical Engineering from Birzeit University, Palestine in 2003, and his DEA and Ph.D. degrees in robotics motion planning from the Polytechnic University of Valencia, Spain in 2006 and 2011, respectively.

In 2012, he began his postdoctoral research at the Jozef Stefan Institute, Slovenia. From 2013 to 2016, he was a Visiting Professor at the Carlos III University of Madrid, Spain. He then held a postdoctoral position at the Istituto Italiano di Tecnologia (IIT) from 2016 to 2019. Between 2019 and 2022, he was a Research Fellow at Aalto University. In 2022, he joined the Technical University of Munich, Germany, as a Senior Scientist and leader of the Robot Learning group at MIRMI. Currently, he is a Lecturer and Researcher at the Faculty of Engineering, Mondragon Unibertsitatea, Spain. His research interests include control theory, differential geometry, and machine learning, with a focus on enhancing robot manipulation performance and safety. Dr. Abu-Dakka has served as an Associate Editor for IEEE-ICRA, IEEE-IROS, and IEEE-RA-L. Webpage: <https://sites.google.com/view/abudakka/>

Matteo Saveriano received his B.Sc. and M.Sc. degrees in Automatic Control Engineering from the University of Naples, Italy, in 2008 and 2011, respectively. He earned his Ph.D. from the Technical University of Munich in 2017. Currently, he is an Assistant Professor at the Department of Industrial Engineering (DII), University of Trento, Italy. He has previously served as an Assistant Professor at the University of Innsbruck and as a Postdoctoral Researcher at the German Aerospace Center (DLR). He is an Associate Editor for RA-L. His research focuses on robot learning, human-robot interaction, and the understanding and interpretation of human activities. Webpage: <https://matteosaveriano.weebly.com/>

Ville Kyrki received his M.Sc. and Ph.D. degrees in Computer Science from Lappeenranta University of Technology, Finland, in 1999 and 2002, respectively. He was a Postdoctoral Fellow at the Royal Institute of Technology, Stockholm, Sweden, from 2003 to 2004, before returning to Lappeenranta University of Technology, where he held various positions from 2003 to 2009. From 2009 to 2012, he served as a Professor of Computer Science at Lappeenranta University of Technology. Since 2012, he has been an Associate Professor of Intelligent Mobile Machines at Aalto University, Helsinki, Finland. His primary research interests are in robotic perception, decision-making, and learning. Dr. Kyrki is a Fellow of the Academy of Engineering Sciences (Finland) and a member of the Finnish Robotics Society and the Finnish Society of Automation. He has held various leadership roles within the IEEE Finland Section, including Chair and Vice Chair of the Jt. Chapter of CS, RA, and SMC Societies, Treasurer, and Co-Chair of the IEEE RAS TC in Computer and Robot Vision. He served as an Associate Editor for the IEEE Transactions on Robotics from 2014 to 2017.



Matteo photo

[Click here to access/download;Photo of the author\(s\);MatteoPic_1.jpg](#)



Ville photo

[Click here to access/download;Photo of the author\(s\);VilleKyrki-227x300.jpg](#) 



Declaration of interests

The authors declare that they have no known competing financial interests or personal relationships that could have appeared to influence the work reported in this paper.

The authors declare the following financial interests/personal relationships which may be considered as potential competing interests:

Journal Pre-proof